Electronic Supplementary Information

The high impact of milling atmosphere on the steel contamination

Goran Štefanić,* Stjepko Krehula and Ivka Štefanić

Ruđer Bošković Institute, Bijenička 54, HR-10000 Zagreb, Croatia

Table of Contents

Section S1 *Reports about steel contamination during the mechanosynthesis of zinc ferrite and some related spinel-type ferrites*

Table S1 The relation between milling conditions and the reports about steel contamination during the mechanosynthesis of zinc ferrite and some related spinel-type ferrites.

Sample	Mill	BPR	Speed* (rpm)	Time/ h	Atmosphere	Product	Report about contamination	Reference
α-Fe_2O_3 + ZnO	Spex 8000	20:1	-	5	air and argon	$ZnFe_2O_4$ (air) (Zn,Fe)O (argon)	Yes/ interaction with sample – reduction of Fe^{3+} ions	10
α-Fe_2O_3 + ZnO	Planetary ball mill AGO 2	20:1	-	0.3	air	Amorphous (RT) $ZnFe_2O_4$ (1100°C)	No	11
α-Fe_2O_3 + ZnO	Planetary ball mill AGO 2	20:1	800	2	air	Amorphous + $ZnFe_2O_4$	No	12
α-Fe_2O_3 + ZnO	Planetary ball mill	20:1	-	630	air/closed container	$ZnFe_2O_4$	No	13
α-Fe_2O_3 + ZnO	Planetary ball mill	20:1	-	1320	air/closed container	$ZnFe_2O_4$	No	14
α-Fe_2O_3 + ZnO	Fritsch P5	20:1	200	50	air	$ZnFe_2O_4$	<1% Cr (EDS)	15
α-Fe_2O_3 + ZnO	Planetary ball mill	20:1	-	90	air	$ZnFe_2O_4$	4.9% Cr (EDS)	16
α-Fe_2O_3 + ZnO	Planetary ball mill AGO 2	20:1	800	2	air	Amorphous + $ZnFe_2O_4$	No	17
α-Fe_2O_3 + ZnO	Fritsch P7	25:1	790	4	air	$ZnFe_2O_4$	No	18
α-Fe_2O_3 + ZnO	Fritsch P5	40:1	325	10	air	$ZnFe_2O_4$	No	19
α-Fe_2O_3 + ZnO	Planetary ball mill	20:1	500	9	air	(Zn,Fe)O + Fe (6 h) spinel (9 h)	Yes/interaction with sample – reduction of Fe^{3+} ions	20
α-Fe_2O_3 + ZnO	Planetary ball mill	20:1	500	40	air	$ZnFe_2O_4$	No	21
α-Fe_2O_3 + ZnO	Spex 8000	20:1	-	12	air	$ZnFe_2O_4$	No	22
α-Fe_2O_3 + ZnO	Fritsch P4	15:1	400	30	air	$ZnFe_2O_4$	2-3% of Fe	23
α-Fe_2O_3 + Zn	Herzog HSM100 oscillating mill	60:1	12.5Hz	0.5	air	$ZnFe_2O_4$	No	24

Table S1 (cont.)

Sample	Mill	BPR	Speed* (rpm)	Time/ h	Atmosphere	Product	Report about contamination	Reference
Fe_3O_4 + Zn	Spex 8000	3.5:1	-	12	argon	Fe + (Zn,Fe)O	~0.5% Fe	25
Fe_3O_4 + Zn	Herzog HSM100 oscillating mill	60:1	12.5Hz	0.5	Air	$ZnFe_2O_4$	No	26
Fe_3O_4 + Zn	Spex 8000	59:1	-	9	argon	Fe + ZnO	~9 at% Fe	27
Fe + Zn + H_2O	Planetary ball mill Resch S1000	10:1	250	22	air/closed container	$ZnFe_2O_4$ (700°C)	No	28
$ZnFe_2O_4$	Spex 8000	3.5:1	-	12	argon	$ZnFe_2O_4$	<0.1% Fe	29
95% ZnO + 5% Fe	Planetary mill QM1SP	35:1	550	80	argon	$Zn_{0.93}Fe_{0.07}O$	2% increase of Fe content	30
ZnO + 10% Fe_2O_3	horizontal oscillatory mill Retsch	11.5:1	32 Hz	16	air and argon	(Zn,Fe)O + $ZnFe_2O_4$	No	31
α-Fe_2O_3	Uni-ball-mill	30:1	-	200	Vacuum	Fe_3O_4	No/ reduction of Fe^{3+} ions due to the breaking of Fe-O bond	32
α-Fe_2O_3	Fritsch P5	20:1	200	240	Air/closed and open container	Fe_3O_4	0.8% Cr / reduction of Fe^{3+} ions due to the breaking of Fe-O bond	S1
α-Fe_2O_3	Planetary ball mill	30:1	-	140	Vacuum, H_2O	Fe_3O_4	No/ reduction of Fe^{3+} ions due to the breaking of Fe-O bond	S2
$CuFe_3O_4$	Fritsch P7	20:1	950	98	air/closed container	$Cu_xFe_{3-x}O_4$ + Fe_3O_4	1.2% Cr / reduction of Fe^{3+} ions due to the breaking of Fe-O bond	S3
α-Fe_2O_3 + NiO	Planetary ball mill AGO 2	20:1	750	0.33	air/closed container	(Ni,Fe)O + Fe + $NiFe_2O_4$	No/ reduction of Fe^{3+} ions due to the breaking of Fe-O bond	S4
α-Fe_2O_3 + MgO	Planetary ball mill	20:1	750	0.3	air	(Mg,Fe)O+Fe + $MgFe_2O_4$	No/ reduction of Fe^{3+} ions due to the breaking of Fe-O bond	S5

Table S1 (cont.)

Sample	Mill	BPR	Speed* (rpm)	Time/ h	Atmosphere	Product	Report about contamination	Reference
Fe_2O_3 + Mn_2O_3	-	8:1	-	110	argon	$MnFe_2O_4$	No/ reduction of Fe^{3+} ions due to the disordering of reactants	S6
α-Fe_2O_3	vertical stainless steel mill	-	-	140	vacuum	$Fe_{3-x}O_4$	2-3% Fe/ reduction of Fe^{3+} ions due to the breaking of Fe-O bond	S7
α-Fe_2O_3 + NiO	Fritsch P5	20:1	~310	50	air	$NiFe_2O_4$	No - decrease of specific electric resistivity	S8
α-Fe_2O_3 + SiO_2	Fritsch P5	20:1	200	365	air/closed container	Fe_3O_4 + Fe^{2+} ions in SiO_2	0.6%.Cr- first sign of Fe after 4 h	S9
α-Fe_2O_3 + ZnO + MnO	Spex 8000	18:5	1200 Hz	40	air	$(Zn,Mn)Fe_2O_4$	Small/ Fe increase linearly with milling time	S10
MnO + Fe_2O_3	Fritsch P5	10:1	320	70	Argon	$MnFe_2O_4$ (35 h) (Fe,Mn)O (50-85h)	Yes/onset of Fe contamination after 35 h of milling attribute to $MnFe_2O_4$	S11
0.88 ZnO + 0.12 FeO	Planetary ball mill	30:1	300	-	air	$(Zn,Fe)O$ + $ZnFe_2O_4$	No	S12
α-Fe_2O_3 + ZnO + MgO	Fritsch P5	40:1	300	25	air	$(Mg,Zn)Fe_2O_4$	No	S13
α-Fe_2O_3 + ZnO + NiO	Planetary ball mill	10:1	600	60	air	$(Zn,Ni)Fe_2O_4$	No	S14
α-Fe_2O_3 + ZnO + NiO	Planetary ball mill	10:1	600	60	air	$(Zn,Ni)Fe_2O_4$	No	S15
α-Fe_2O_3 + ZnO + NiO	Fritsch P5	20:1	-	50	air	$Ni_xZn_{1-x}Fe_2O_4$	No	S16

* Most reports related to planetary ball-mills did not specify whether the mentioned rotation speed refers to the main disk or vials. However it is more likely that the speed refers to the main disc, because this value is usually shown on the display of the mill.

Section S2 *Chemicals and Synthesis*

The starting material was ultra-pure zincite powder, produced by *Ventron*. Milling was performed using the *Fritsch* planetary ball mill Pulverisette 6. In the milling we used ten steel balls (ball diameter = 10 mm) and steel bowl of 80 cm^3. The results of EDS analysis (see Section S11 *EDS analysis*) show that the steel balls contain ~98.5% of Fe and ~1.5% of Cr, while the steel bowl contain ~71% of Fe, ~21% of Cr, ~6% of Ni and smaller amounts of other elements (C, Mn, Mo, Si). Significant difference in the Cr/Fe ratio of the steel balls and steel bowl made it possible to identify the source of contamination (whether it comes from the balls or from a bowl) (see Table S5). The main disk rotation speed was 500 rpm and the powder-to-ball weight ratio 1:20. The milling time varied from 1 to 30 hours. After each full hour, milling stopped for 10 minutes to allow cooling of the milling assembly.

In order to examine the influence of more or less oxidative atmospheres, three milling procedures were used (A, B and C). In the procedure A milling was performed in the air atmosphere. After each hour of milling bowl was left with open lid and the sample was stirred for 5 minutes in order to introduce a fresh air. A small amount of samples (~50 mg) were taken at selected times for analysis. In the procedures B and C, the initial zinc powder was milled for 14 and 30 hours without opening the container during the cooling process. In the procedure B closed milling was performed in air atmosphere, while in the procedure C closed milling was performed in the nitrogen atmosphere. For thermal stability study, the products obtained after 30 h of ball-milling (samples A30, B30 and C30) were subjected to temperature treatment at 500 °C and 1000 °C for 2 h. Structural and microstructural changes in the ball-milled zincite were investigated at room temperature (RT) using X-ray powder diffraction (XRD), ^{57}Fe Mössbauer spectroscopy, field emission scanning electron microscopy (FE SEM), energy dispersive X-ray spectrometry (EDS), thermogravimetric (TG) analysis and UV-Vis-NIR spectroscopy. The notation of the samples and the results of phase are given in Table S2.

Section S3 *Instruments and Characterization*

XRD measurements were taken using an *ItalStructure*s diffractometer APD2000 with monochromatized CuK_α radiation (graphite monochromator). XRD patterns were scanned in 0.02^o steps (2θ), in the 2θ range from 15° to 105°, with a fixed counting time (15 s). Rietveld refinements[s17] (program MAUD[s18]) of powder diffraction patterns were used for a quantitative crystal phase analysis of ball-milled products. With the exception of the pure zincite (R_{wp} = 0.108), the weighted residual error indexes (R_{wp}) of all the refined patterns were less than 10%. The obtained results are given in Table S2 and Figs. 3 and S8. Precise lattice parameters of the zincite- and franklinite-type products (Table S3, Fig. S12) were determined from the results of Le Bail refinements of powder diffraction patterns[s19] (program GSAS[s20] with a graphical user interface EXPGUI[s21]). Silicon (*Koch-Light Lab. Ltd.*) was used as an internal standard (space group $Fd\bar{3}m$; a = 5.43088 Å; JCPDS-ICDD PDF card No. 27-1402). The physical broadening (β) of the most prominent diffraction lines was used to estimate the volume-averaged domain size (D_v) and the root-mean-square strain (ε_{RMS}) according to the so-called 'double-Voigt' method[s22] equivalent to the Warren-Averbach approach[s23]. This method, in which Voigt functions were used to describe the contribution of both the crystallite size and the lattice micro-strain to the broadening of the diffraction lines, was performed by using the computer program BREADTH[s24]. Physically broadened line profiles (β) were obtained by convolution-fitting approach (program SHADOW[s25]) in which the instrumental profile (diffraction lines of the starting zincite powder) is convoluted with a refineable Voigt function to fit the observed profile (diffraction lines of ball-milled samples). The results of diffraction line broadening analysis are summarized in Fig. S9.

[57]Fe Mössbauer spectra were recorded at 20 °C in the transmission mode using a standard *WissEl (*Starnberg, Germany) instrumental configuration. A [57]Co/Rh Mössbauer source was used. The velocity scale and all data refer to the metallic α-Fe absorber at 20 °C. A quantitative analysis of the recorded spectra was made using the *MossWinn* program.

FE SEM/EDS analyses of uncoated samples were made using the field emission scanning electron microscope JSM-7000F (JEOL) equipped with an energy dispersive X-ray spectrometer INCA-350EDS Microanalysis System (*Oxford Instruments*). In the EDS analysis we used accelerating voltage of 15 kV and probe current of 10 nA. In order to obtain better statistic EDS

analysis were performed at low magnifications. The results of elemental analysis of the milled samples were based on several (at least three) independent EDS measurements.

Thermogravimetric (TG) analysis of the samples was performed in air up to 1000 °C with a scanning rate of 5 K min‑1 using a DTG-60H Thermal Analyzer (Shimadzu Scientific Instruments Inc.). The instrument was connected to a personal computer loaded with a program for processing the obtained TG curves.

Diffuse reflectance UV-VIS-NIR spectra were obtained at 20 °C using a Shimadzu UV-VIS-NIR spectrometer (model UV-3600) equipped with an integrated sphere. Barium sulfate was used as reference.

Section S4 *Colors of the Products*

Fig. S1 Color of the starting zincite (ZnO) and the products obtained after ball-milling of zincite by using procedure A (samples A1, A2, A5, A9, A14, A20, A30, A30-500 and A30-1000) and procedure B (samples B30, B30-500 and B30-1000)
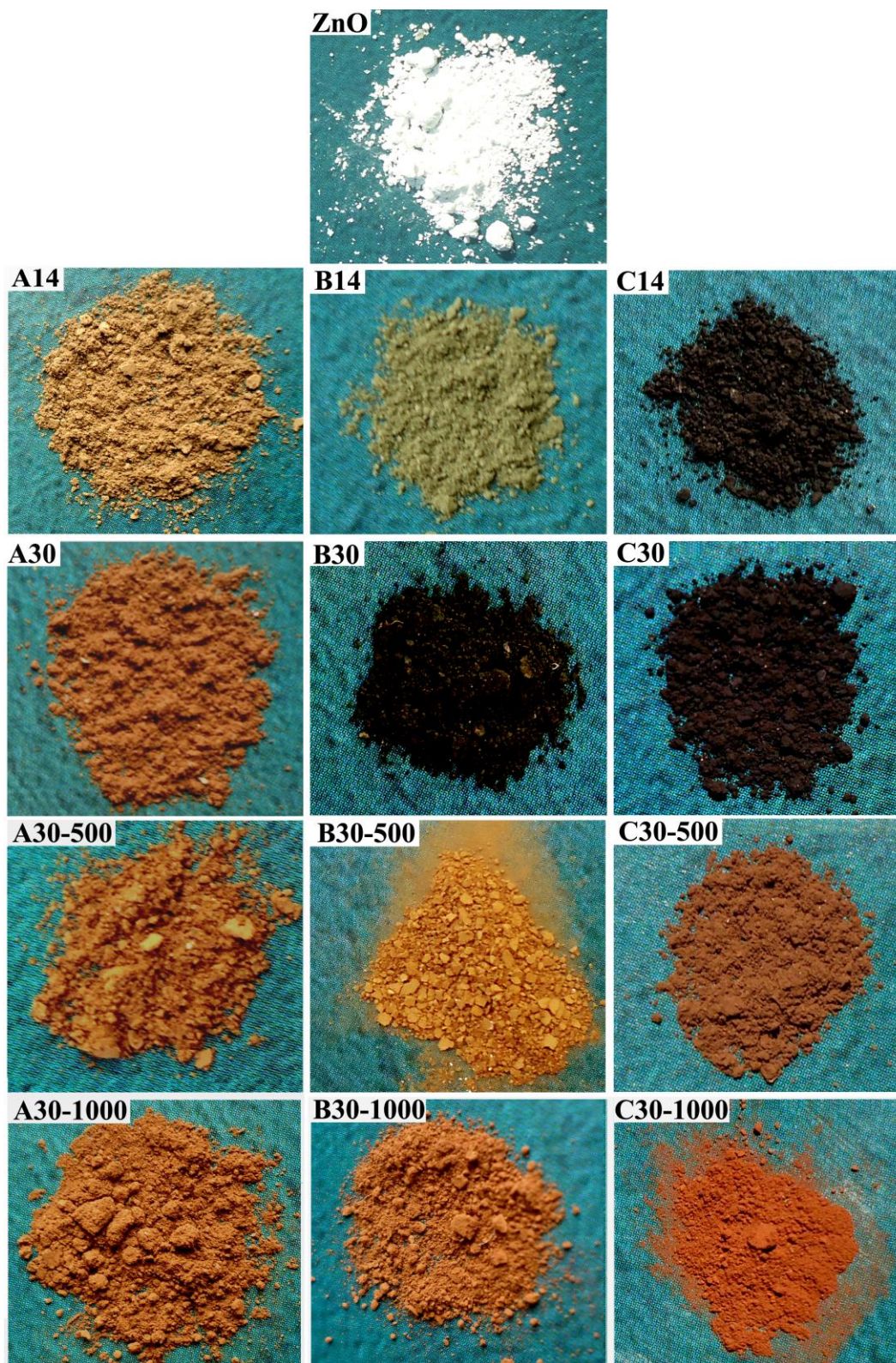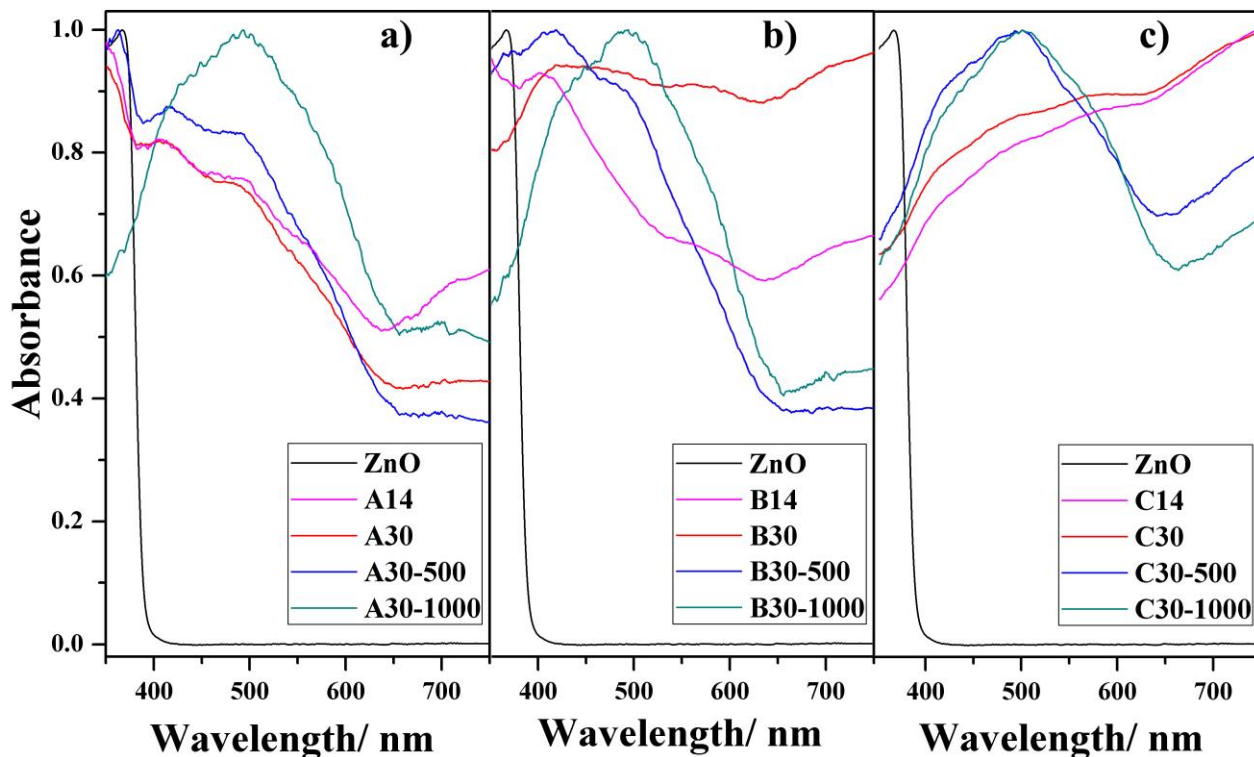
Fig S2 Color of the starting ZnO and the products obtained after 14 and 30 h of ball-milling by using procedure A, B and C and calcination of the final milling product (30 h) at 500 and 1000 °C.

The result of UV-VIS diffuse reflectance spectroscopy shows that starting zincite (ZnO) is transparent in the visible region of spectrum with characteristic band gap absorption edge at ~365 nm (3.4 eV). Samples B30, C14 and C30 (black) exhibit continuous absorption in the whole visible region of spectrum, while the spectra of sample A30 and the products of obtained after calcinations of samples A30, B30 and C30 exhibit band gap absorption edge at ~650 nm (1.91 eV) typical for franklinite ($ZnFe_2O_4$).[S26] Increase in wavelength of the absorption maximum of sample B30-1000 compared to the sample B30-500 is connected with the change in the color of those calcination products from yellowish-brown (product obtained after calcination of sample B30 at 500 °C) to red-brown (product obtained after calcination of sample B30 at 1000 °C).

Fig. S3 UV-VIS spectra of the starting zincite (ZnO) and the products obtained after 14 and 30 h of ball-milling by using procedure A, B and C and calcination of the final milling product at 500 and 1000 °C.

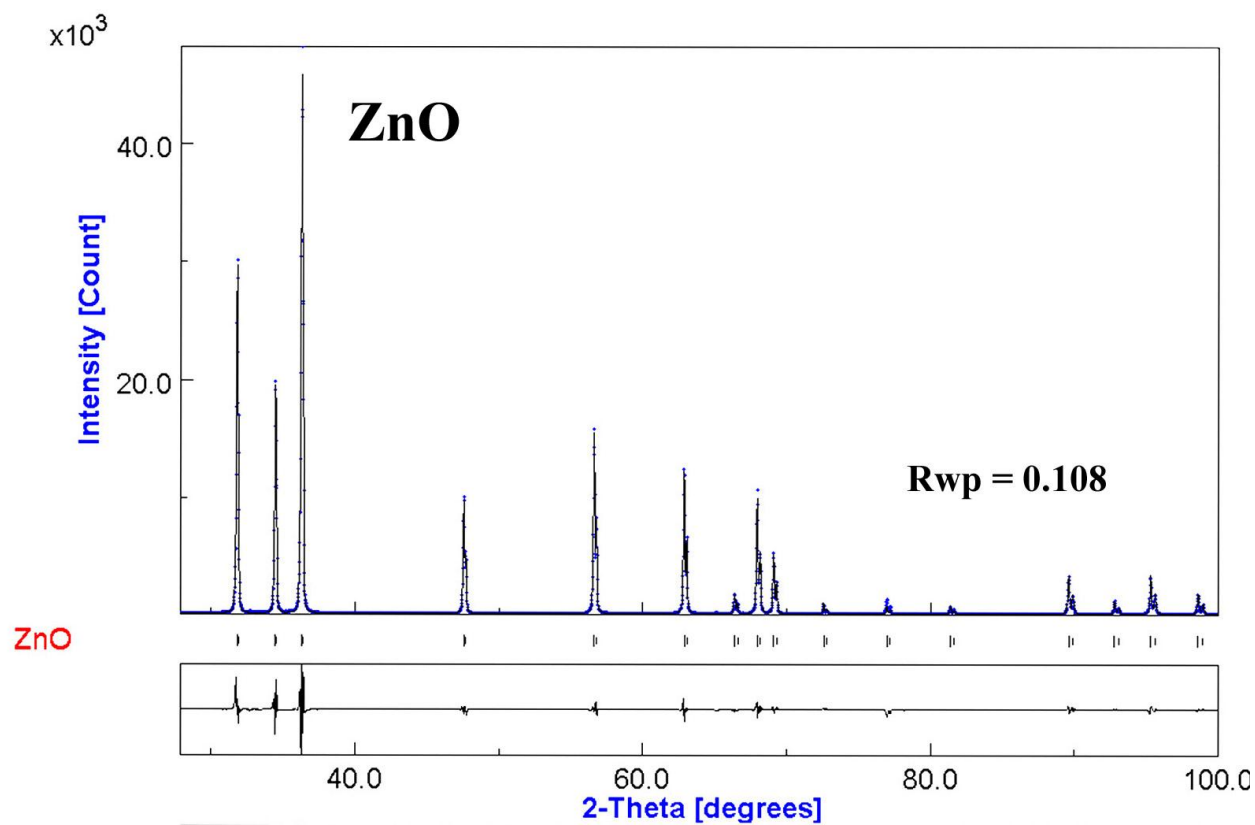**Section S5** *Quantitative Crystal Phase Analysis*

Fig. S4 Rietveld refinements on powder diffraction patterns of the starting zincite (ZnO). The difference between the observed and calculated patterns is shown in the box below.
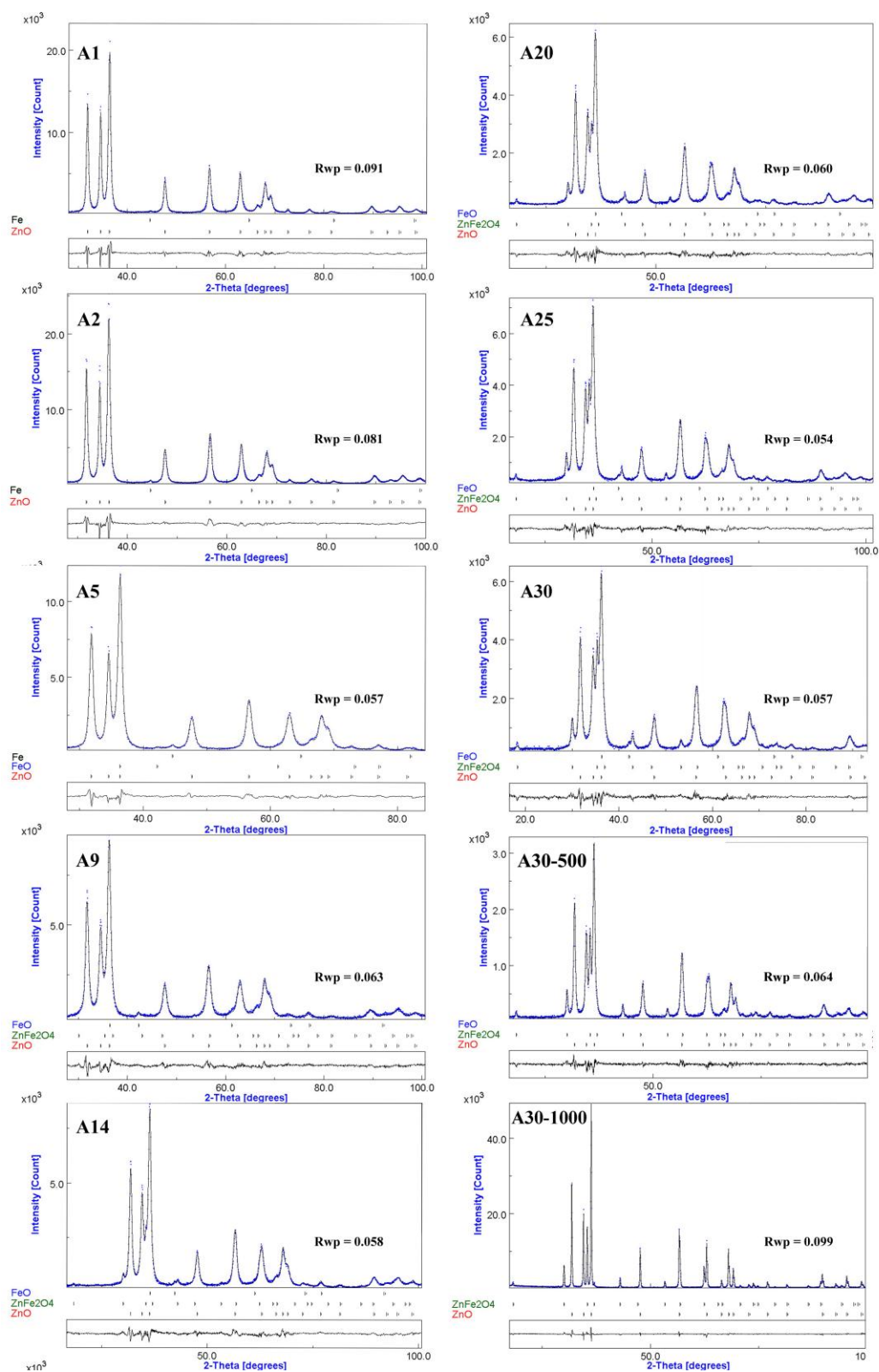
Fig. S5 Rietveld refinements on powder diffraction patterns of the products obtained by using procedures A (samples A1, A2, A5, A9, A14, A20, A25, A30, A30-500 and A30-1000). The difference between the observed and calculated patterns is shown in the box below.
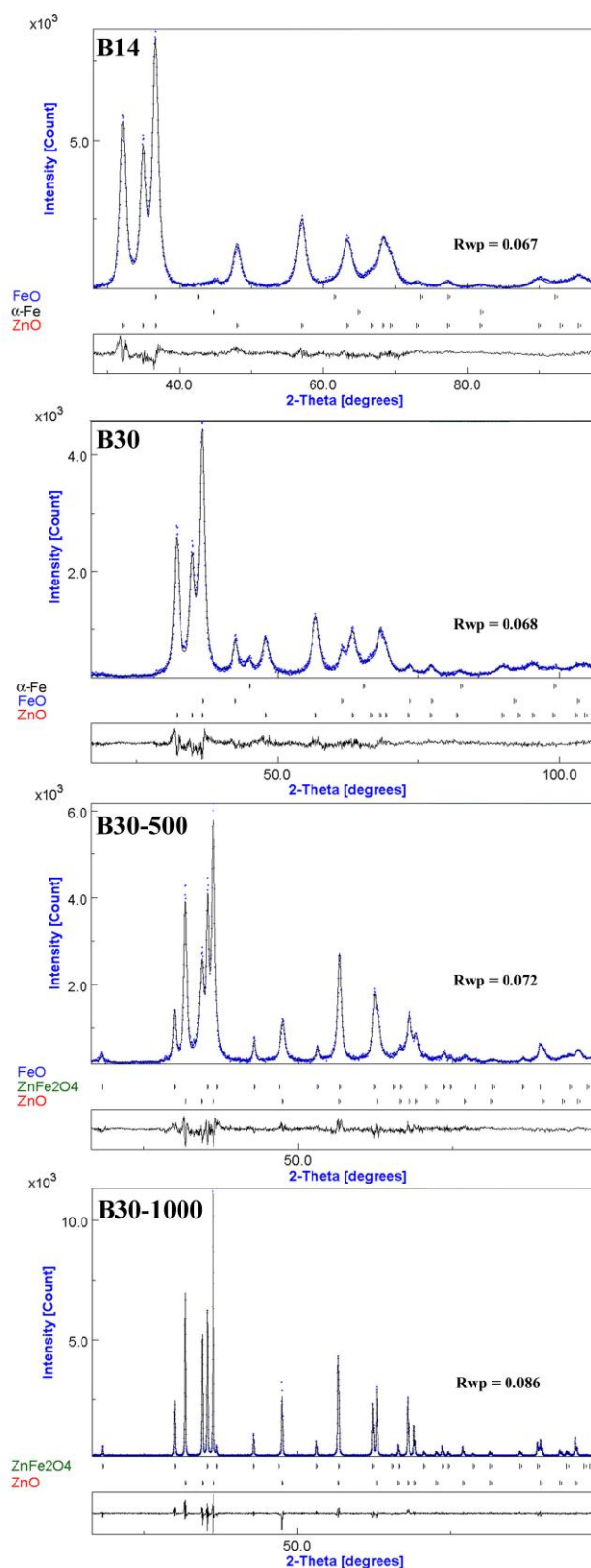
Fig. S6 Rietveld refinements on powder diffraction patterns of the products obtained by using procedures B (samples B14, B30, B30-500 and B30-1000). The difference between the observed and calculated patterns is shown in the box below.
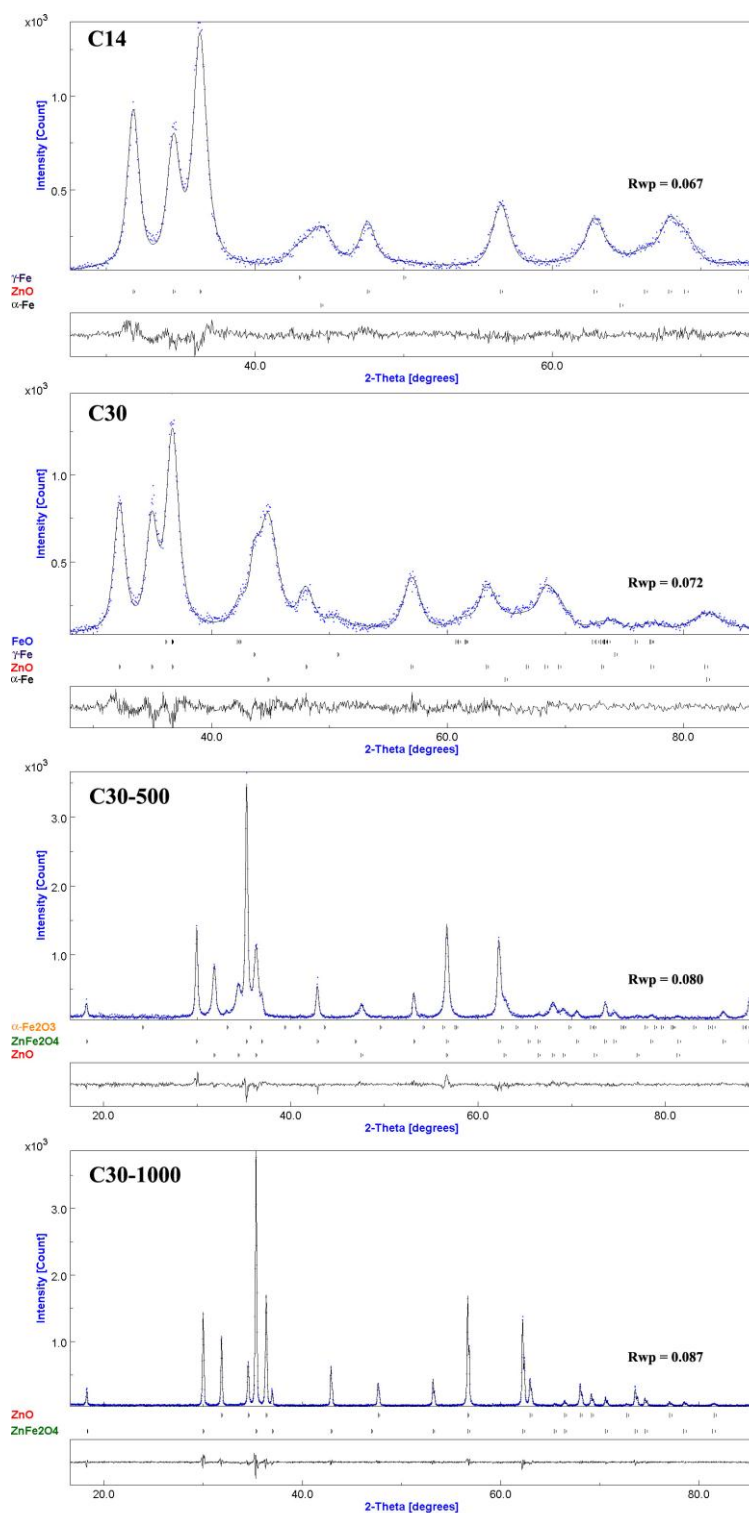
Fig. S7 Rietveld refinements on powder diffraction patterns of the products obtained by using procedures C (samples C14, C30, C30-500 and C30-1000). The difference between the observed and calculated patterns is shown in the box below.
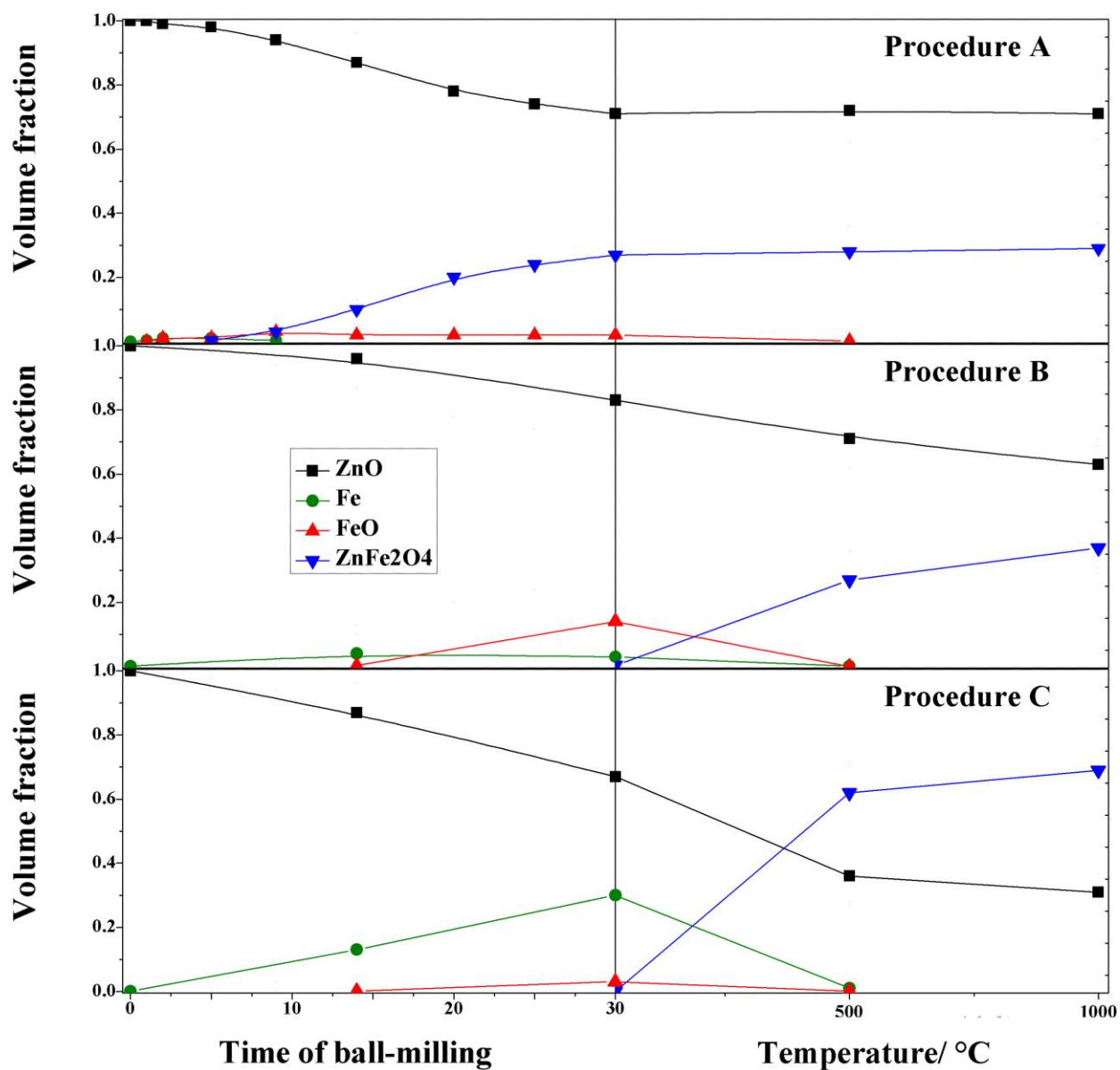
Fig. S8 The influence of ball-milling of pure zincite by using the procedures A, B and C and temperature treatment of the final milling product (30 h) on the phase composition as determined from the results of Rietveld refinements of the powder diffraction patterns.

Table S2

The results of quantitative crystal phase analysis of the products obtained upon ball-milling and calcination of zincite powder by following the procedures A, B and C. The volume fraction of the obtained crystalline phases was determined from the results of Rietveld refinements.

Sample	Time of ball-milling	Temperature	Phase composition (volume fraction)	Rwp
ZnO	-	RT	ZnO	0.108
A1	1 h	RT	Z	0.091
A2	2 h	RT	$Z(0.99) + \alpha\text{-}Fe$ (0.01)	0.081
A5	5 h	RT	Z (0.98) + $\alpha\text{-}Fe$ (0.01) + W (0.01)	0.057
A9	9 h	RT	Z (0.95) + F (0.03) + W (0.02)	0.063
A14	14 h	RT	Z (0.88) + F (0.11) + W (0.01)	0.058
A20	20 h	RT	Z (0.78) + F (0.20) + W (0.02)	0.060
A25	25 h	RT	Z (0.75) + F (0.23) + W (0.02)	0.054
A30	30 h	RT	Z (0.71) + F (0.27) + W (0.02)	0.057
A30-500	30 h	500 °C	Z (0.72) + F (0.28)	0.064
A30-1000	30 h	1000°C	Z (0.71) + F (0.29)	0.099
B14	14 h	RT	Z (0.97) + Fe (0.03)	0.067
B30	30 h	RT	Z (0.83) + W (0.14) + Fe (0.03)	0.068
B30-500	30 h	500 °C	Z (0.71) + F (0.29)	0.072
B30-1000	30 h	1000 °C	Z (0.63) + F (0.37)	0.086
C14	14 h	RT	Z (0.87) + $\alpha\text{-}Fe$ (0.09) + γ-Fe (0.04)	0.067
C30	30 h	RT	Z (0.67) + $\alpha\text{-}Fe$ (0.23) + γ-Fe (0.07) + W (0.03)	0.072
C30-500	30 h	500 °C	F (0.62) + Z (0.36) + H (0.02)	0.080
C30-1000	30 h	1000 °C	F (0.70) + Z (0.30)	0.087

Description: Z = phase structurally similar to zincite (ZnO), $\alpha\text{-}Fe$ = phase structurally similar to alpha iron, $\gamma\text{-}Fe$ = phase structurally similar to gamma iron, W = phase structurally similar to wüstite (FeO), F = phase structurally similar to franklinite (ZnFe$_2$O$_4$), H = phase structurally similar to hematite (α-Fe$_2$O$_3$)

Section S6 *Diffraction line-broadening (size-strain) analysis*

The results of the line broadening analysis of the products obtained by procedure A show a significant decrease in the volume-averaged domain size (D_v) and an increase in the root-mean-square strain (ε_{RMS}) in the first five hours of milling (Fig. S9). Lattice micro-strains reached maximum values after ~9 h of ball-milling. Further ball-milling up to 14 h causes a small decrease in strain, while crystallite size remains almost unchanged. Further ball-milling up to 30 h has a very small influence on both the crystallite size and the lattice strains of zincite-type products. In case of the products obtained after 14 h and 30 h of ball-milling by the procedures B and C, the results of line broadening analysis indicate significant increase of the ε_{RMS} values compare to the values obtained for the corresponding products obtained by procedure A. The D_v values of the products obtained after 14 h and 30 h of ball-milling by the procedures B and C appeared to be almost the same as those obtained by the procedure A (~10 nm). The obtained D_v values appeared to be significantly smaller compared to the particle sizes observed in the FE-SEM micrographs of the corresponding products (see Section S10). Temperature treatments of the final products (30 h) obtained by procedures A, B and C cause an increase of D_v and a decrease of ε_{RMS} values (Fig. S9).
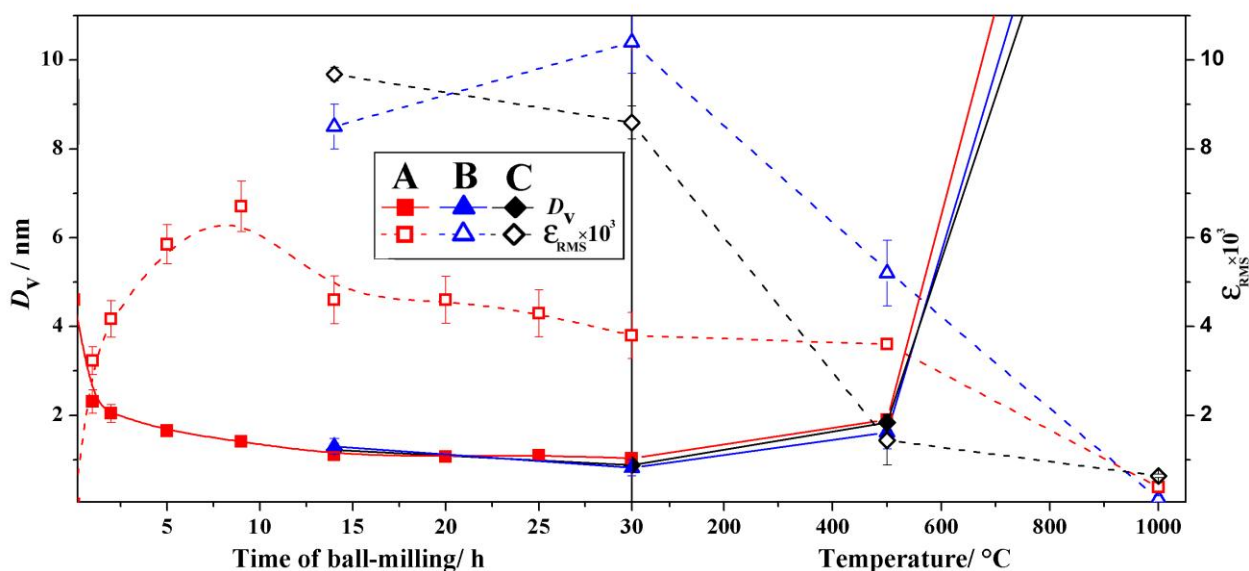

Fig. S9 The influence of ball-milling of pure zincite and temperature treatment of the final milling product (30 h) on the volume-averaged domain size (D_v, full symbols) and the root-mean-square strain (ε_{RMS}, empty symbols) of the obtained products.

17
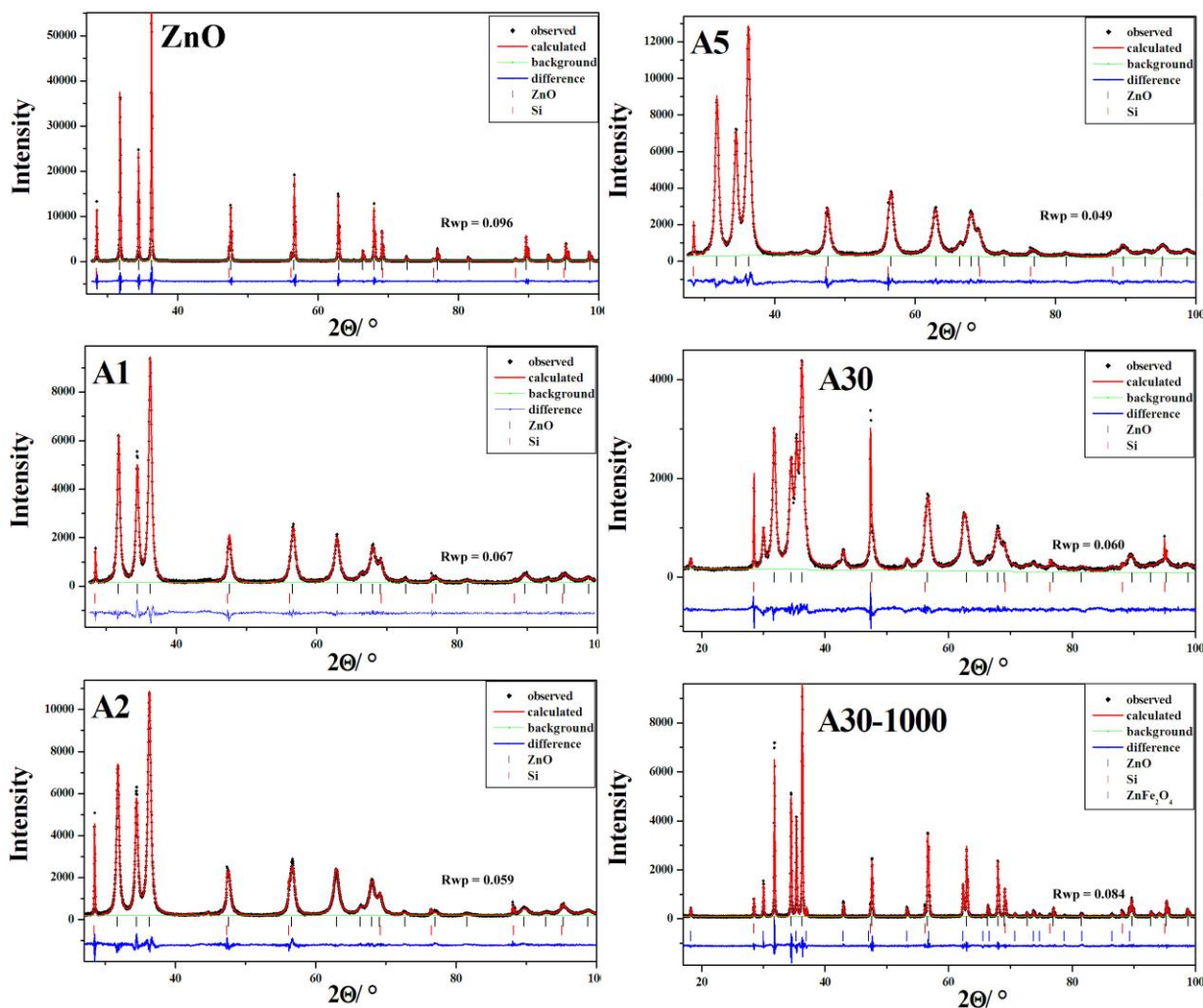
Section S7 *Unit-cell Parameters*

Fig S10 Le Bail refinements on powder diffraction patterns of the starting ZnO and the products obtained by using procedures A (samples A1, A2, A5, A30 and A30-1000) and silicon as an internal standard. The difference between the observed and calculated patterns is shown as a line in the lower field.
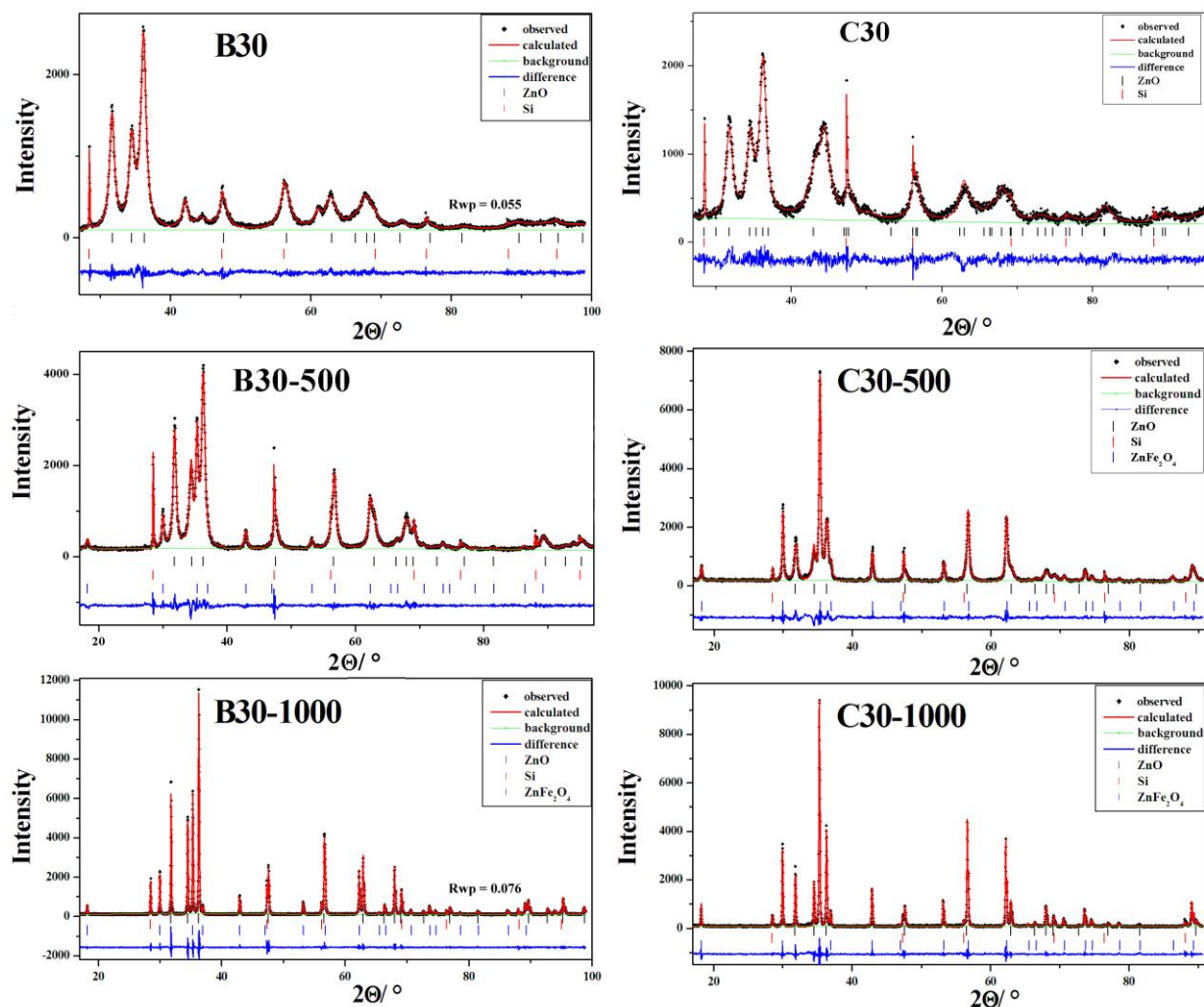
Electronic Supplementary Material (ESI) for Chemical Communications
This journal is © The Royal Society of Chemistry 2012

Fig S11 Le Bail refinements on powder diffraction patterns of the products obtained by using procedures B and C (samples B30, B30-500 and B30-1000, C30, C30-500 and C30-1000) and silicon as an internal standard. The difference between the observed and calculated patterns is shown as a line in the lower field.

Table S3

Refined values of unit-cell parameters of the zincite- and franklinite-type phases as determined from the results of Le Bail refinements on powder diffraction patterns with added silicon as an internal standard.

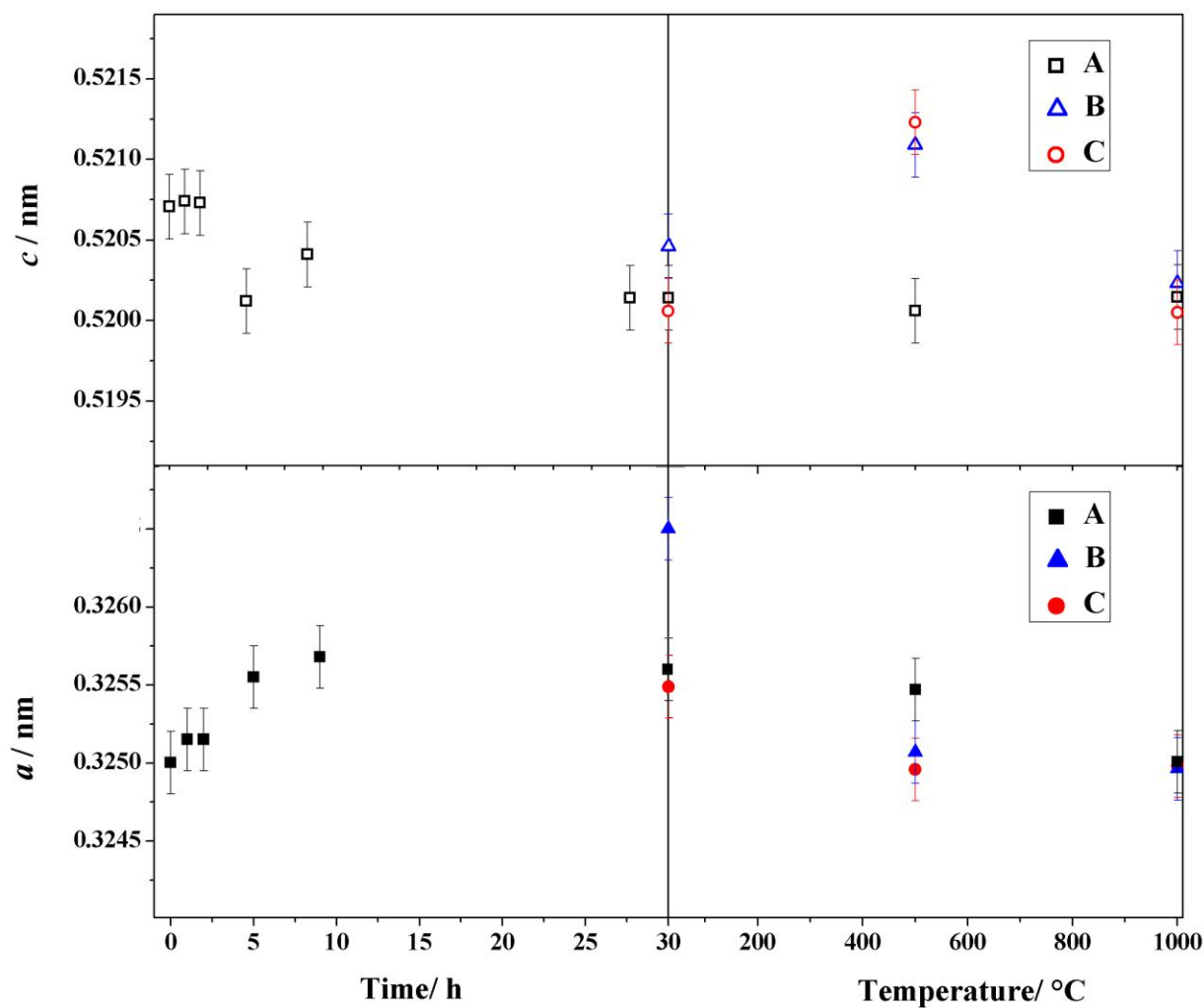| Sample	Lattice parameters			R_{wp}
	Zincite		Franklinite	
	a / nm	c / nm	a / nm	
ZnO	0.325003(2)	0.520707(4)	-	0.096
A1	0.32515(1)	0.52074(3)	-	0.067
A2	0.32515(1)	0.52073(2)	-	0.060
A5	0.32555(1)	0.52012(3)	-	0.045
A9	0.32568(2)	0.52041(5)	-	0.057
A30	0.32560(2)	0.52014(5)	0.84208(5)	0.060
A30-500	0.32547(1)	0.52006(3)	0.84188(4)	0.064
A30-1000	0.325009(2)	0.520146(6)	0.84207(1)	0.084
B30	0.32650(3)	0.52046(8)	-	0.055
B30-500	0.32506(2)	0.52109(4)	0.84314(3)	0.058
B30-1000	0.324962(2)	0.520233(5)	0.84314(7)	0.096
C30	0.32549(7)	0.52006(12)	-	0.070
C30-500	0.32496(2)	0.52123(4)	0.84358(1)	0.075
C30-1000	0.32498(1)	0.52005(2)	0.84406(2)	0.097

Fig. S12 The influence of ball-milling time (up to 30 h) and the temperature treatments of the final milling product on the lattice parameters a (full symbols) and c (empty symbols) of the zincite-type phase as determined from the results of Le Bail refinements. Black squares, blue triangles and red circles represent parameters of the products obtained by using procedure A, B and C, respectively.

Section S8 *Mössbauer spectroscopy*

The results of Mössbauer spectroscopy show that, while in the case of products from series A an almost complete oxidation to Fe(III) occurs during the milling process (Figs. 2 and S13, Table S4), iron contaminations in sample B30 are present in all three oxidation states (Fe(II) is dominant) and in many different surroundings (Figs. 2, S13 and S14, Table. S4). A very broad Fe(II) doublet in the spectrum of sample B30 was best fitted using a distribution of quadrupole splitting, which indicates the presence of many different environments of Fe(II) ions in the sample. The isomer shift of 0.92 mm s^{-1} is in line with literature data for Fe(II) in wüstite.[s27] The presence of the Fe(III) doublet in the spectrum is in line with the fact that stoichiometric wüstite (FeO) cannot exist as a stable phase at atmospheric pressure and that the part of Fe(III) ions is always present.[s27] The formula of non-stoichiometric wüstite can therefore be written as Fe(II)$_{1-3x}$Fe(III)$_{2x}$O. A portion of Fe(II) and Fe(III) ions is likely to be incorporated into the ZnO structure and this type of solid solution is reported in literature.[s28-s30] Heating of sample B30 at 500 ℃ caused oxidation of all iron atoms to the oxidation state +3. The best fit of the Mössbauer spectrum was obtained using two Fe(III) doublets. The inner doublet is similar to the spectrum of sample B30-1000 and to the spectra of highly crystalline normal spinel $ZnFe_2O_4$ obtained by the ceramic method reported in literature.[29,s31,s32] The outer doublet with a somewhat lower isomer shift (0.31 mm s^{-1}) and a large line width can be attributed to the contribution of Fe(III) ions in the tetrahedral lattice sites[s31,s32] and/or the sites connected with a zincite-type solid solution as indicated by the results of XRD analysis. Mössbauer spectrum of the sample C30 consists of two sextets correspond to Fe(0) in α-Fe (first with narrow lines and high HMF corresponds to bulk α-Fe, second with broad lines and distribution of HMF corresponds to nanocrystalline α-Fe), one singlet corresponds to Fe(0) in γ-Fe and one doublet corresponds to Fe(II) in wüstite. The spectrum of sample C30-1000 is similar to the spectra of highly crystalline normal spinel $ZnFe_2O_4$ obtained by the ceramic method reported in literature. [29,s31,s32]
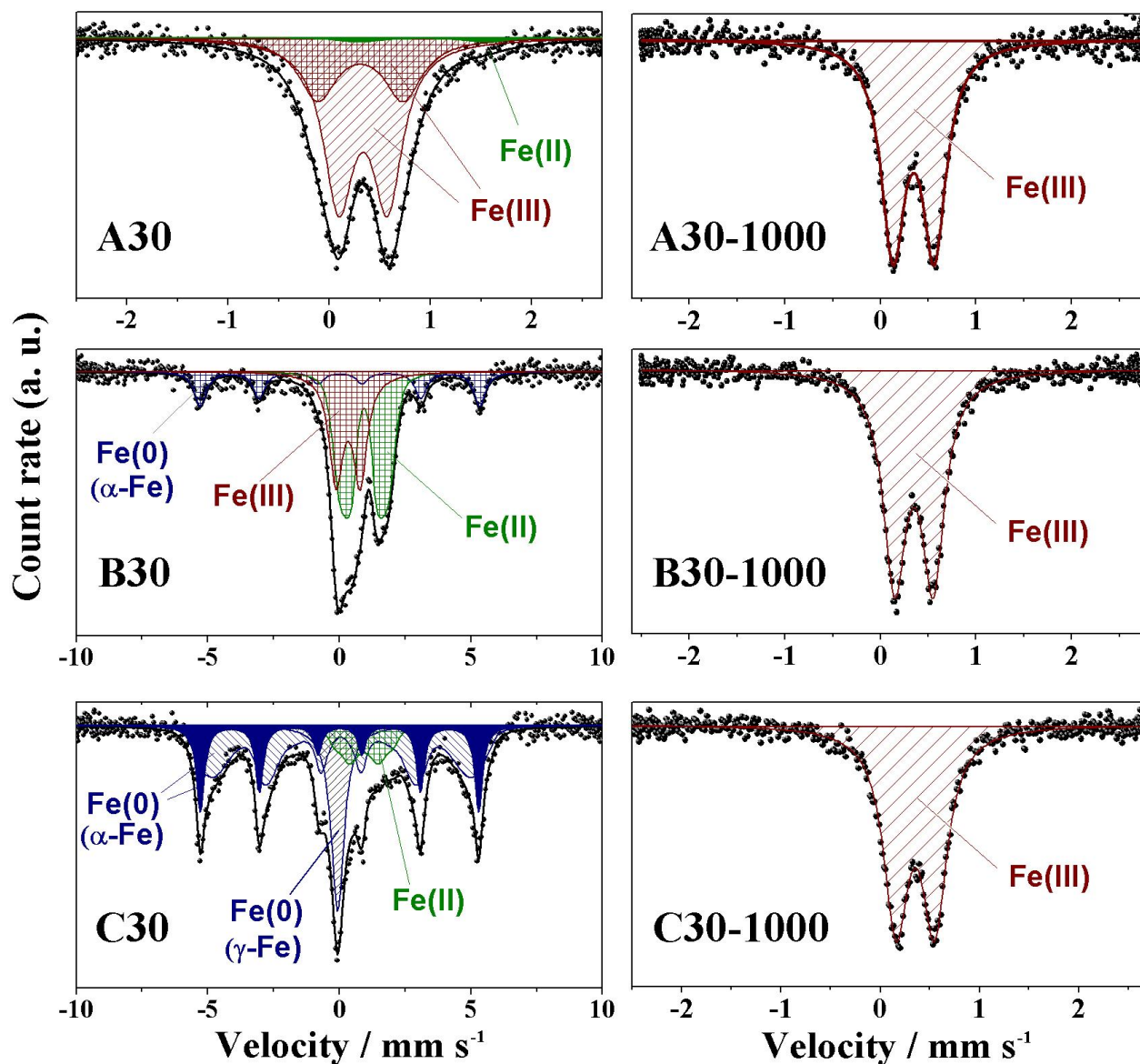
Fig. S13 Mössbauer spectra of the products obtained after 30 h of ball-milling by using the procedures A, B and C (samples A30, B30 and C30) and temperature treatment of this milling products at 1000 °C (samples A30-1000, B30-1000 and C30-1000).
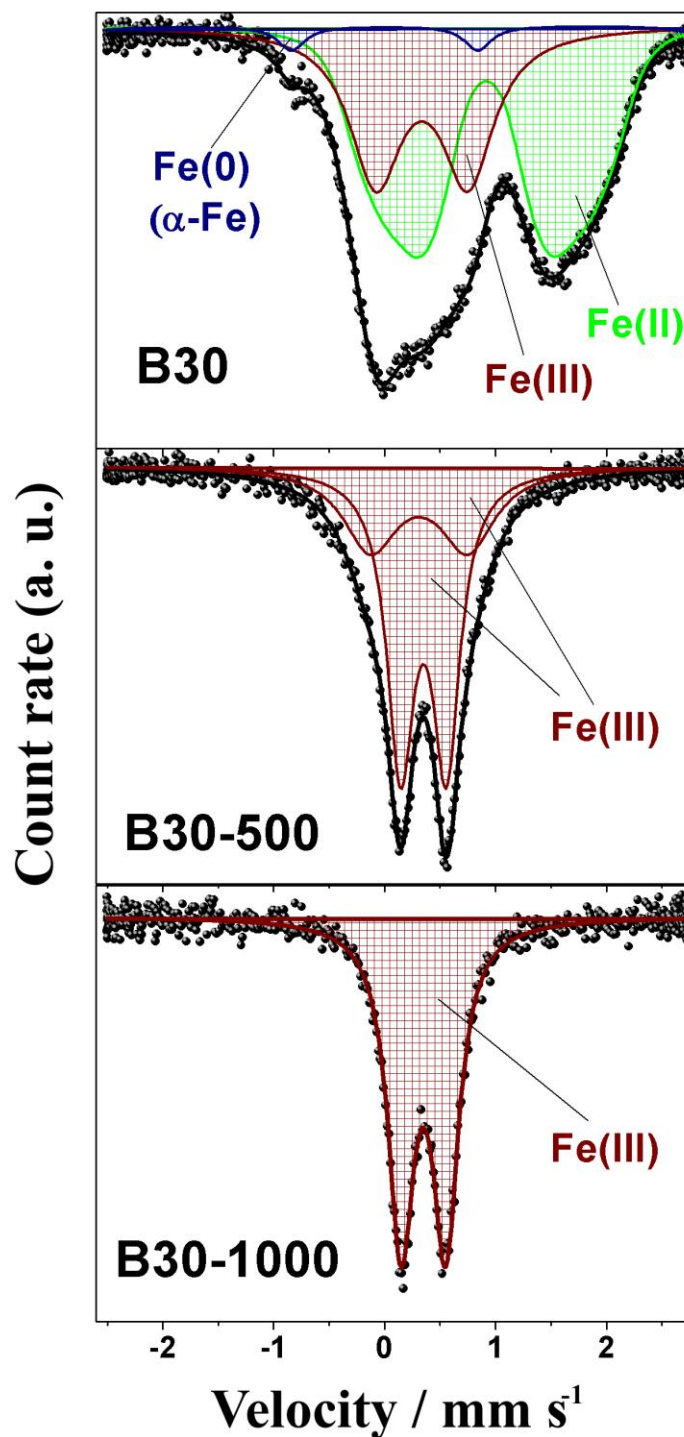
Fig. S14 Characteristic part of Mössbauer spectra of the products obtained after 30 h of ball-milling by using the procedures B (sample B30) and temperature treatment of this milling products at 500 °C and 1000 °C (samples B30-500 and B30-1000).

Table S4 [57]Fe Mössbauer parameters calculated for selected samples and identification.

Sample	Spectral line	δ (mm s^{-1})	Δ (mm s^{-1})	B_{hf} (T)	Γ (mm s^{-1})	Area (%)	Identification
A30	Q	0.34	0.48	-	0.36	66.2	Fe(III)
	Q	0.31	0.85	-	0.45	31.2	Fe(III)
	Q	0.92	1.26	-	0.50	2.6	Fe(II)
A30-1000	Q	0.35	0.43	-	0.30	100.0	Fe(III)
B30	Q	0.92	1.49*	-	0.27	54.8	Fe(II)
	Q	0.34	0.83	-	0.57	29.9	Fe(III)
	M	0.00	-	33.0	0.30	15.3	α-Fe
B30-500	Q	0.35	0.41	-	0.30	64.2	Fe(III)
	Q	0.31	0.87	-	0.60	35.8	Fe(III)
B30-1000	Q	0.35	0.40	-	0.29	100.0	Fe(III)
C30	M	0.01	-	32.8	0.37	23.6	α-Fe
	M	0.07	-	28.0**	0.41	46.5	α-Fe
	S	- 0.06	-	-	0.59	19.5	γ-Fe
	Q	0.93	1.29*	-	0.35	10.3	Fe(II)
C30-1000	Q	0.35	0.39	-	0.30	100.0	Fe(III)

Errors: $\delta = \pm 0.01$ mm s^{-1}, $\Delta = \pm 0.01$ mm s^{-1}, $B_{hf} = \pm 0.2$ T.

Isomer shift is given relative to α-Fe.

* Mean value of a distribution of quadrupole splitting

** Mean value of a distribution of hyperfine magnetic field

Section S9 *Thermal Gravimetric Analysis*

TG curves of the starting zincite (ZnO) and the sample A30 show continuous loss of mass during the heating up to 1000 °C. In case of starting zincite more pronounced mass loss occurs in the region between 200 and 270°C due to the loss of water and carbon dioxide.[s33] Zincite powder stored in the atmosphere could absorb considerable amounts of H_2O and CO_2.[s34] Differently from samples A0 and A30, TG curve of samples B30 and C30 show increase in the mass in the temperature region between 300°C and 700°C connected with the oxidation of iron and chromium contaminations. However, the increase of the samples mass appeared to be five times bigger in case of the sample C30 (increase of 13.7% of starting mass) compared to the sample B30 (increase of 2.7% of starting mass), indicating a significant increase of the steel contamination during the milling by procedure C (Fig. S15). Further increase of the temperature caused a small decrease of the mass due to the zincite evaporation[s35]. Evaporation of zinc at high temperature caused a small increase in the amounts of iron and chromium contaminations as observed by the results of EDS analysis (Fig. S41).
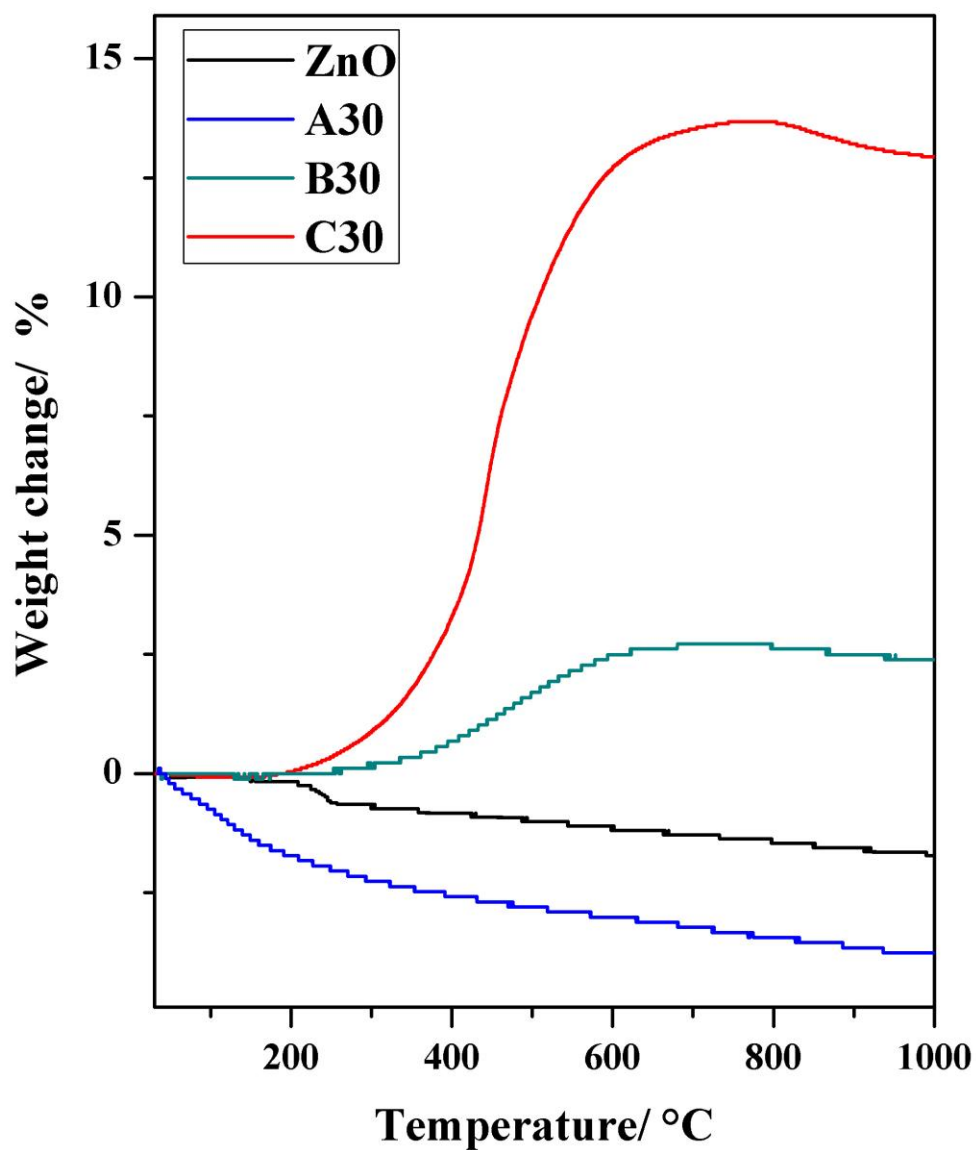
Fig S15 The results of thermogravimetric analysis of starting ZnO and the products obtained after 30 h of ball-milling by using procedure A (sample A30), B (sample B30) and C (sample C30).

Section S10 *FE-SEM analysis*

The results of FE-SEM analysis show that the ball-milling of the starting zincite by the procedure A caused a significant decrease of the particle in the first 5 h of milling (from 100-500 nm to 10-30 nm). Further milling has very small influence on the particle sizes. Differently from the procedure A, prolonged milling (30 h) in the less oxidative atmosphere (procedure B) resulted in the increase of the particle sizes. Increase of the particle sizes become much more pronounced after prolonged milling by the procedure C.
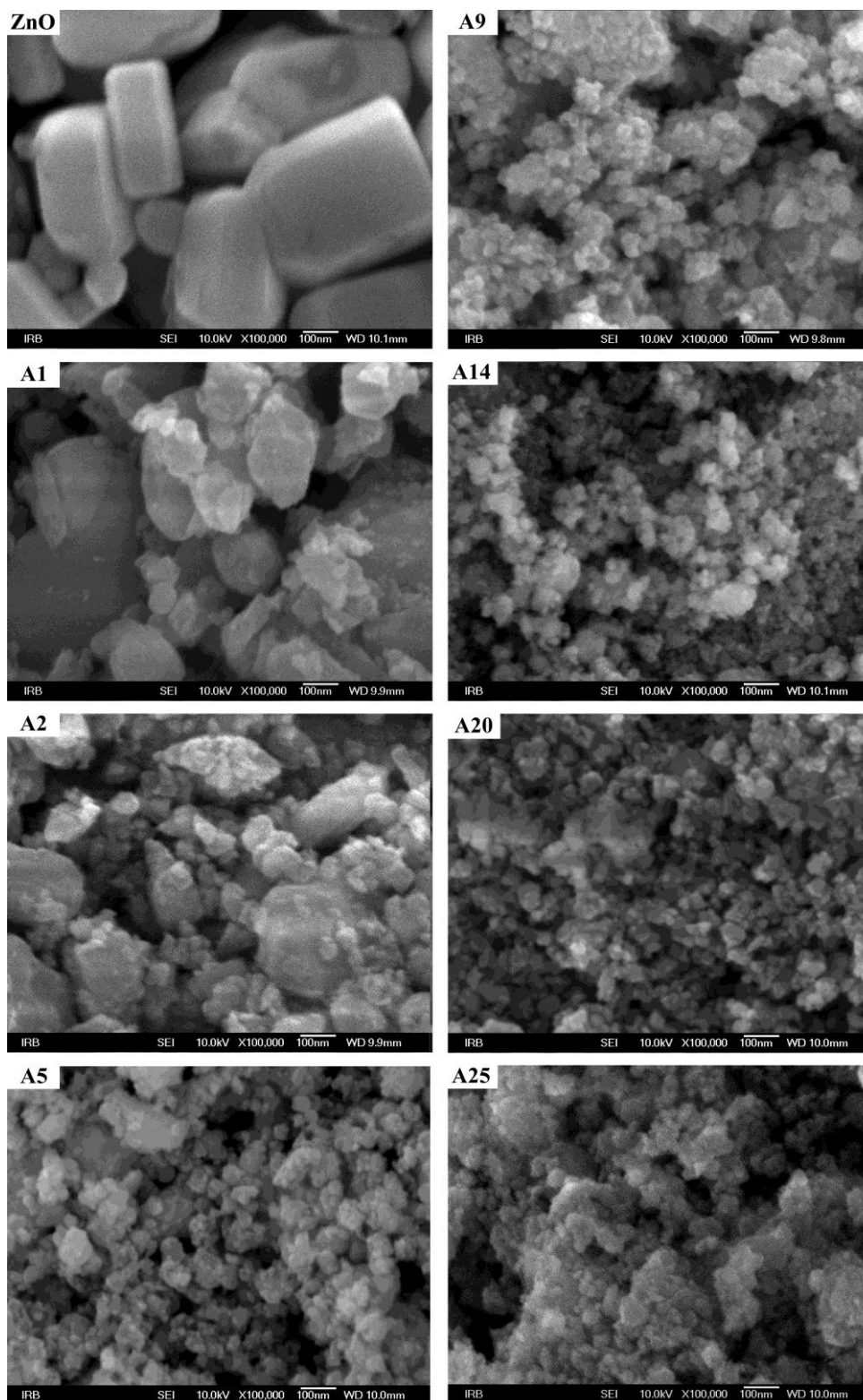
Fig S16 FE-SEM micrographs at 100 000 × magnification of starting zincite (ZnO) and the products obtained after 1 h, 2 h, 5 h, 9 h, 14 h, 20 h and 25 h of ball-milling using procedure A (samples A1, A2, A5, A9, A14, A20 and A25).
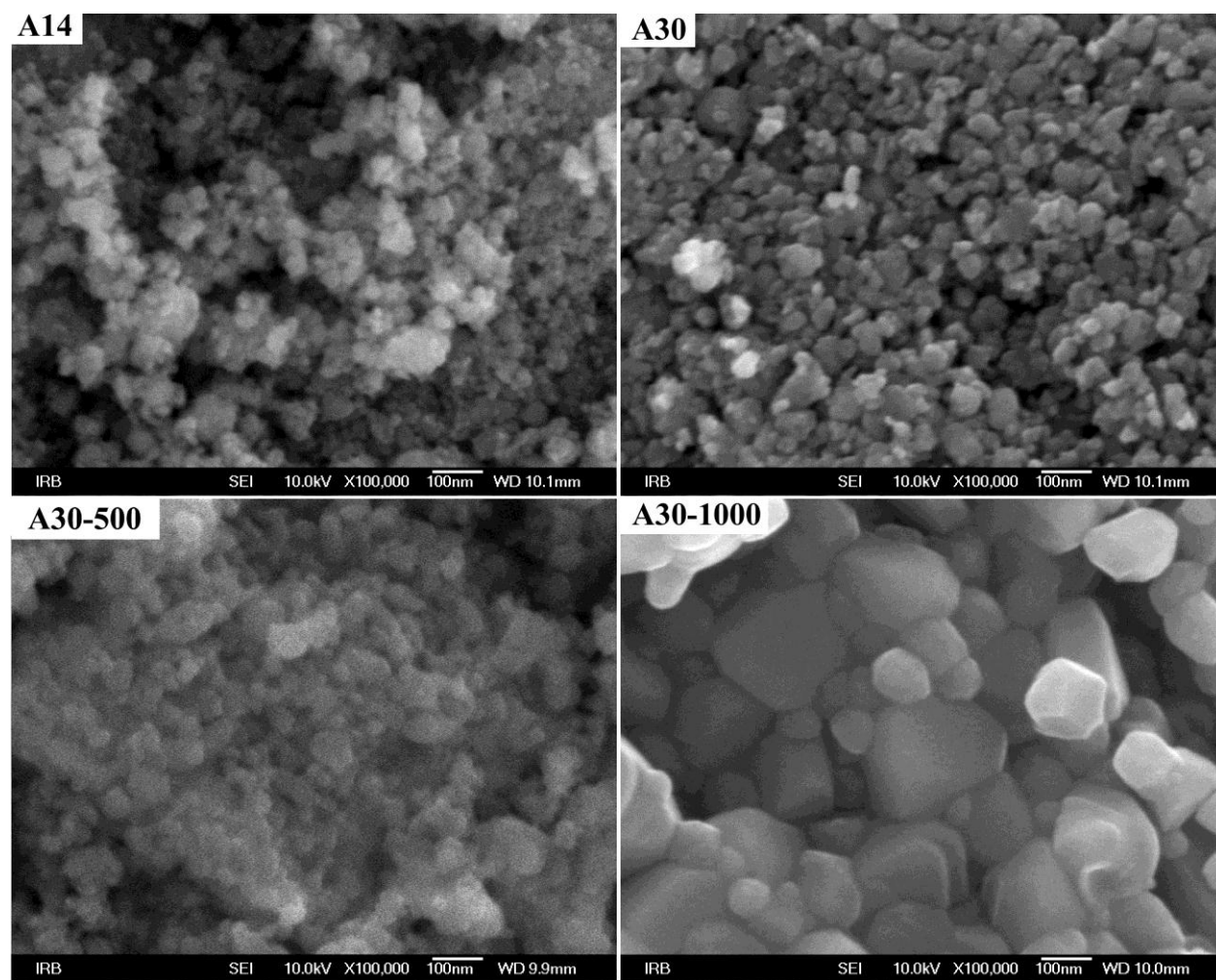
Fig S17 FE-SEM micrographs at 100 000 × magnification of the products obtained after 14 h and 30 h of ball-milling using procedure A (sample A14 and A30) and the products obtained after calcination of sample A30 at 500°C and 1000 °C (samples A30-500 and A30-1000).

Fig S18 FE-SEM micrographs at 100 000 × magnification of the products obtained after 14 h and 30 h of ball-milling using procedure B (sample B14 and B30) and the products obtained after calcination of sample B30 at 500°C and 1000 °C (samples B30-500 and B30-1000).
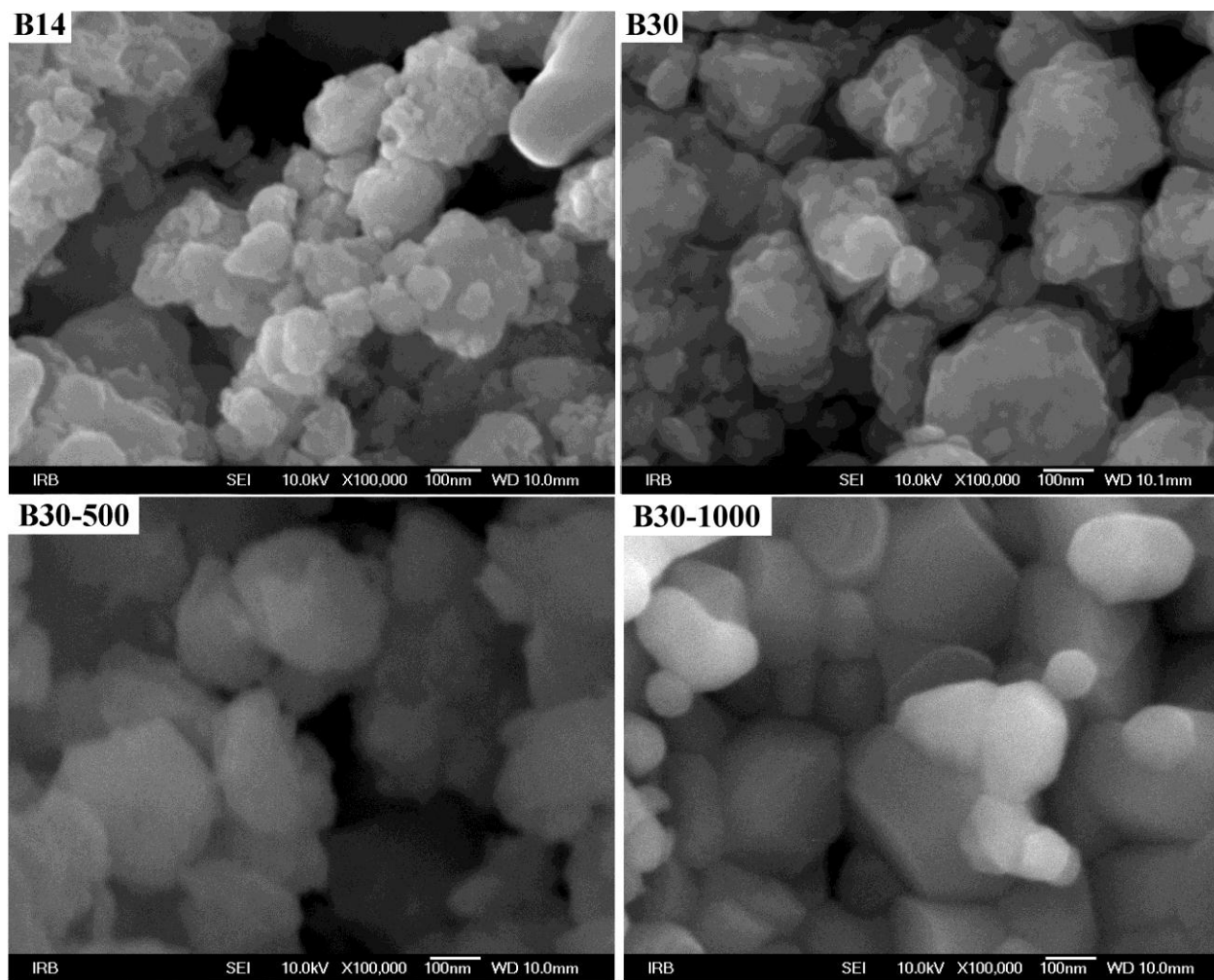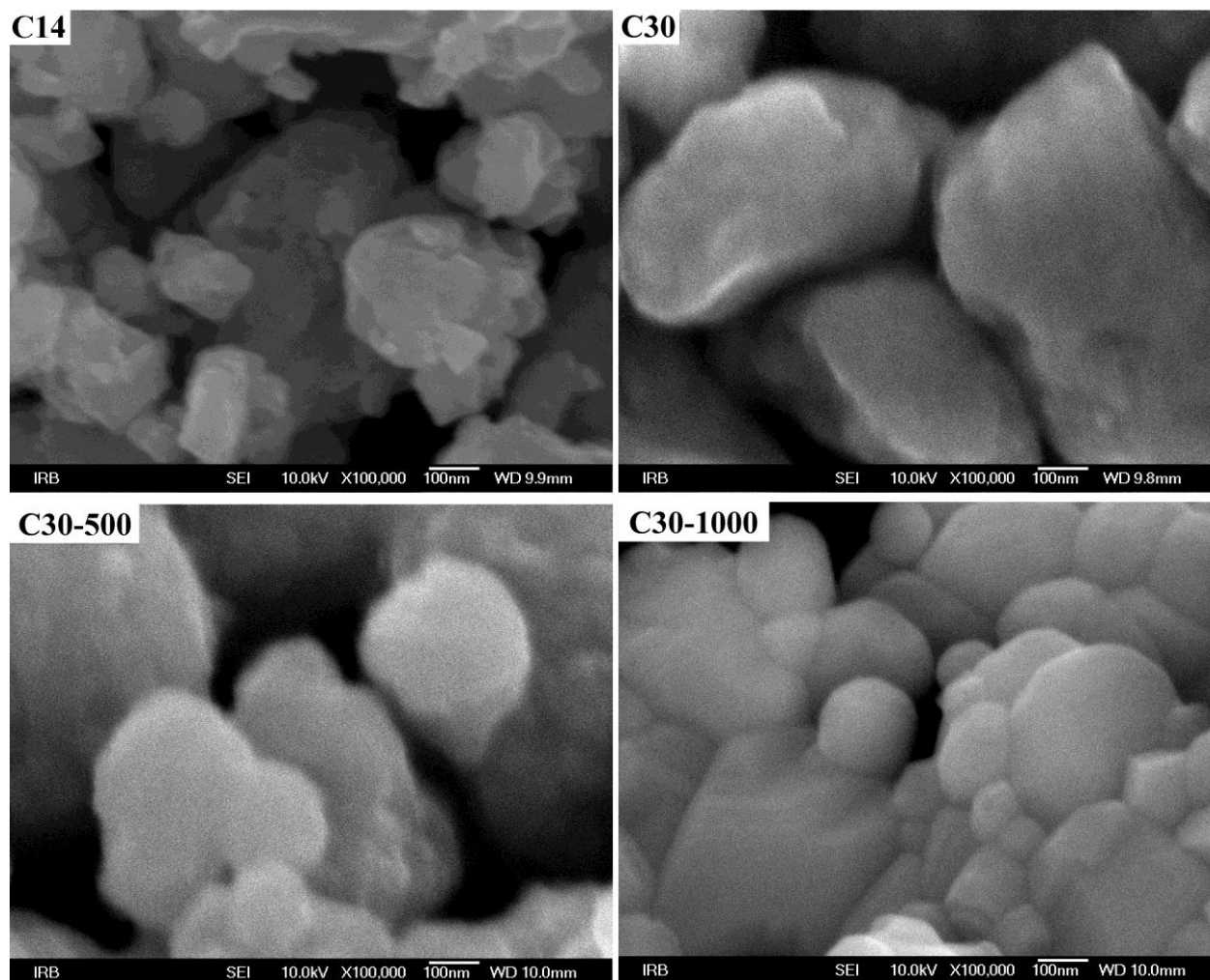
Fig S19 FE-SEM micrographs at 100 000 × magnification of the products obtained after 14 h and 30 h of ball-milling using procedure C (sample C14 and C30) and the products obtained after calcination of sample C30 at 500°C and 1000 °C (samples C30-500 and C30-1000).
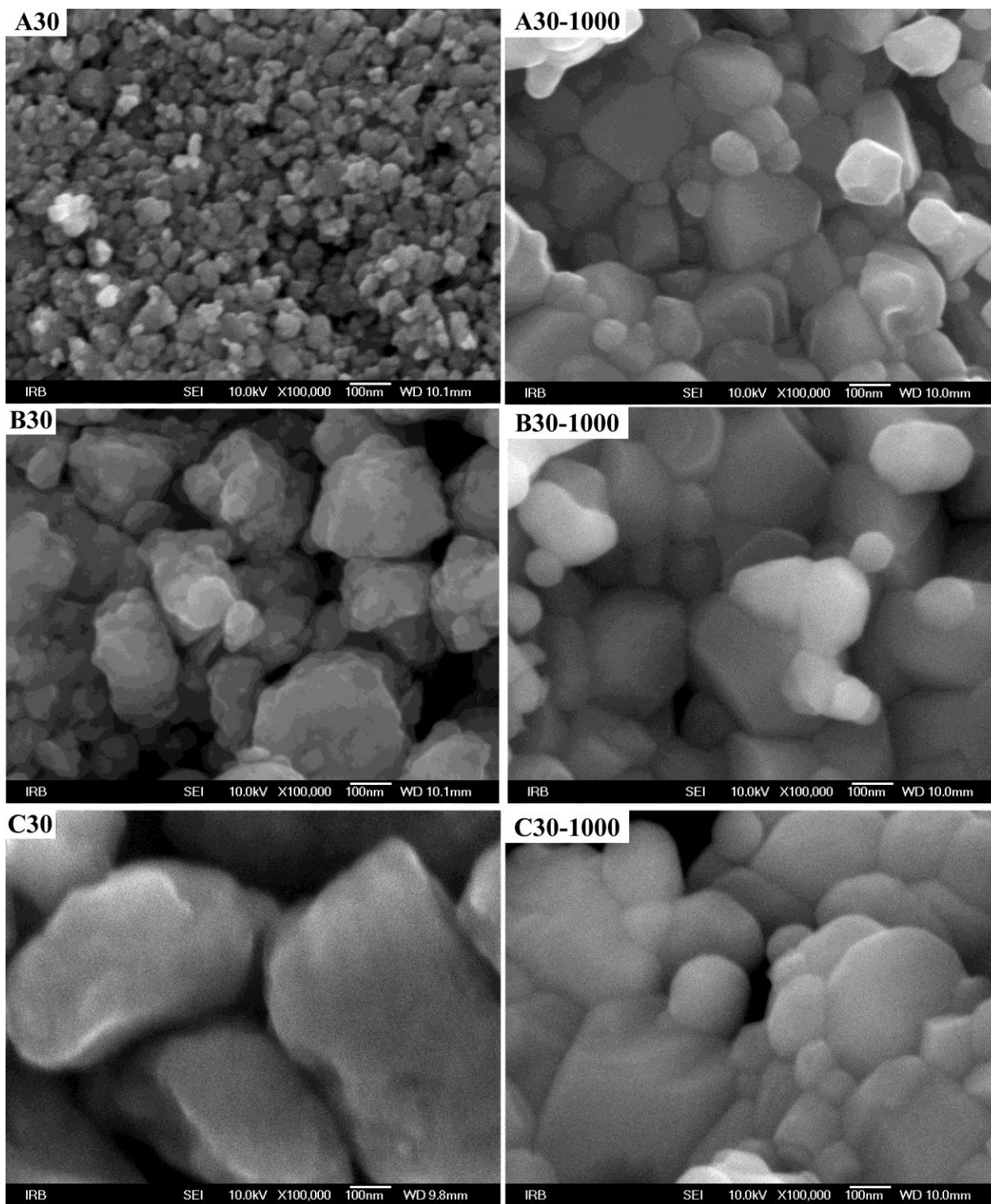
Fig S20 FE-SEM micrographs at 100 000 × magnification of the products obtained after 30 h of ball-milling using procedure A (sample A30), procedure B (sample B30) and procedure C (sample C30) and the corresponding products of calcination at 1000 °C (samples A30-1000, B30-1000 and C30-1000).

Section S11 *EDS analysis*

The results of elemental analysis of the milled samples were based on several (at least three) independent EDS measurements performed at low magnification. In case of sample A2 we also made EDS analysis at higher magnification (Fig. S24) that shows presence of individual steel particle, coming into the sample due to the wear of milling tools.
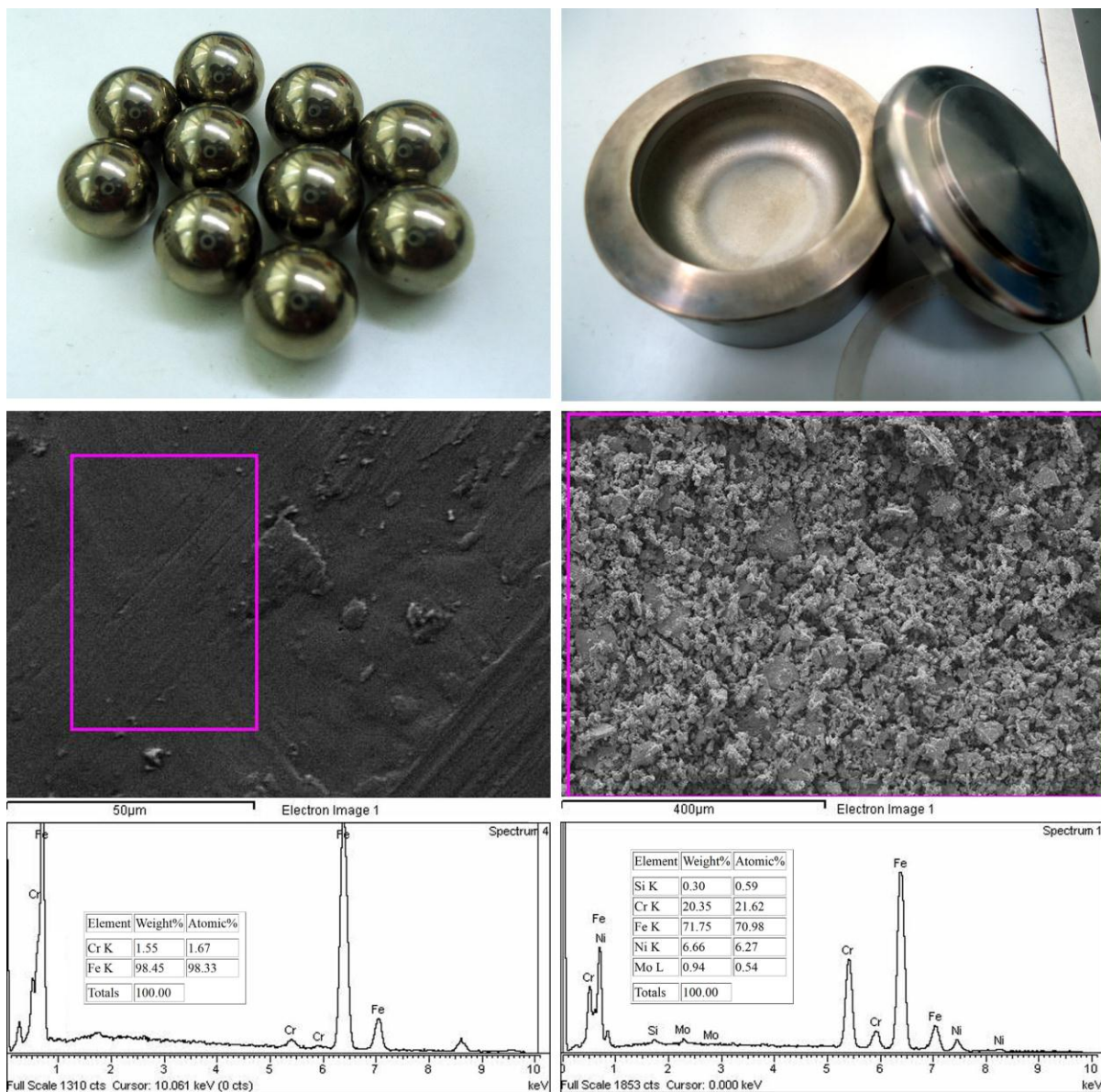
Fig. S21 FE-SEM micrographs and the corresponding EDS spectra of milling balls (left) and steel chips coming from milling bowl (right). Inset tables show the results of elemental analysis.

Element	Weight%	Atomic%
O K	20.04	50.59
Zn K	79.96	49.41
Totals	100.00	
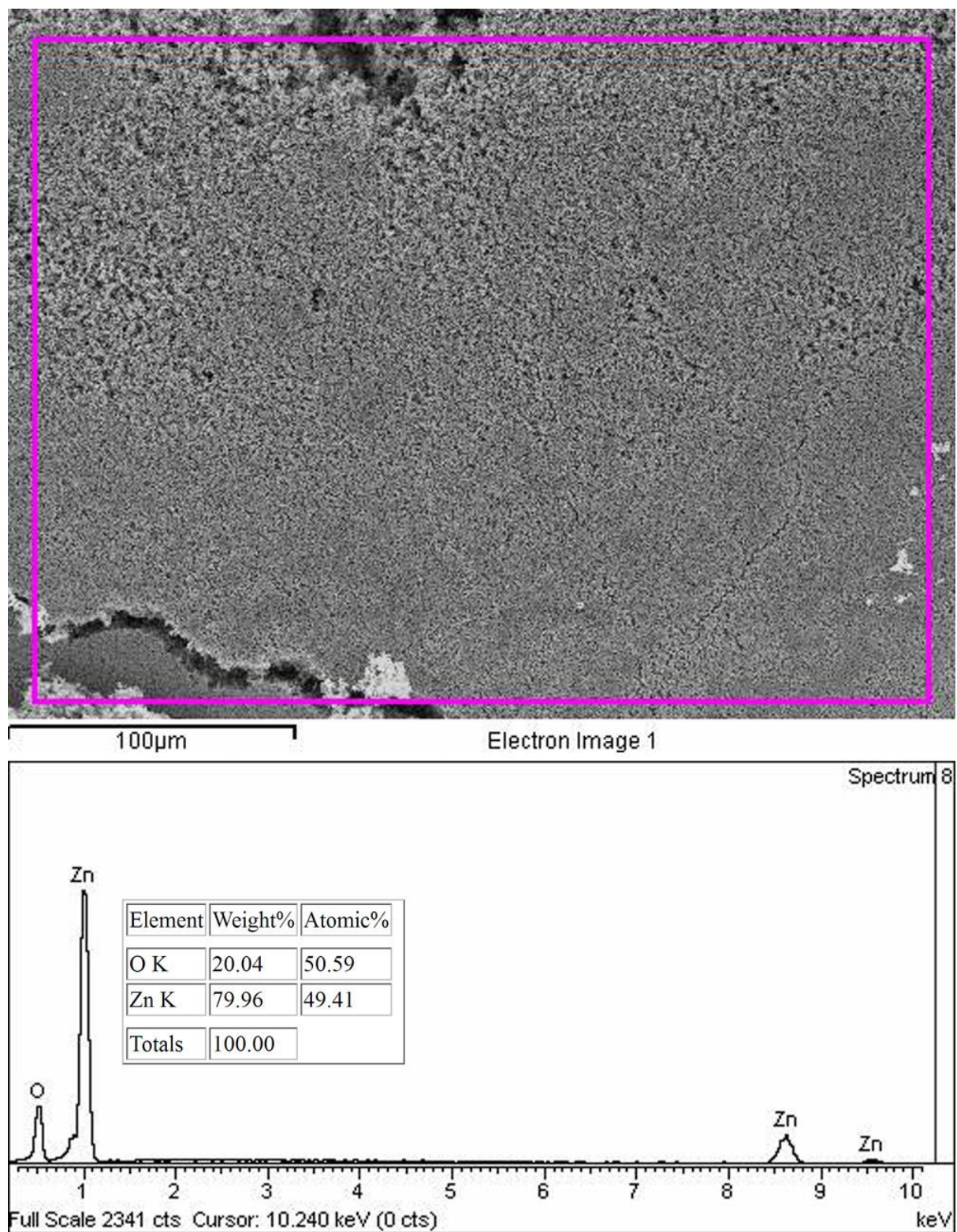
Fig. S22 FE-SEM micrograph of starting zincite (ZnO) powder obtained at $300 \times$ magnification (top) and the corresponding EDS spectrum (bottom). Inset table shows the results of elemental analysis.

Element	Weight%	Atomic%
O K	14.69	41.23
Fe K	1.52	1.22
Zn K	83.79	57.55
Totals	100.00	
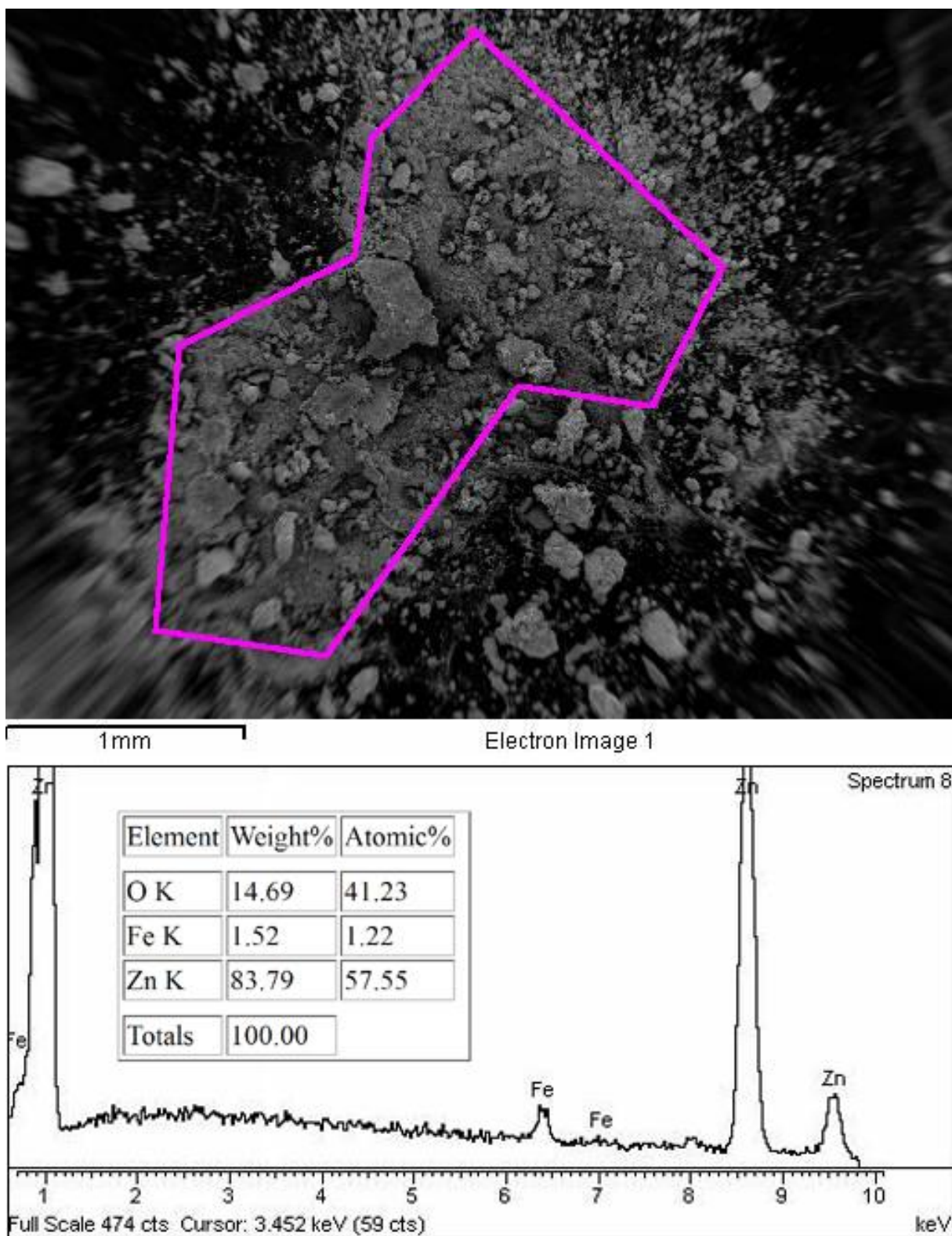
Fig. S23 FE-SEM micrograph of sample A2 obtained at 25 × magnification (top) and the corresponding EDS spectrum (bottom). Inset table shows the results of elemental analysis.
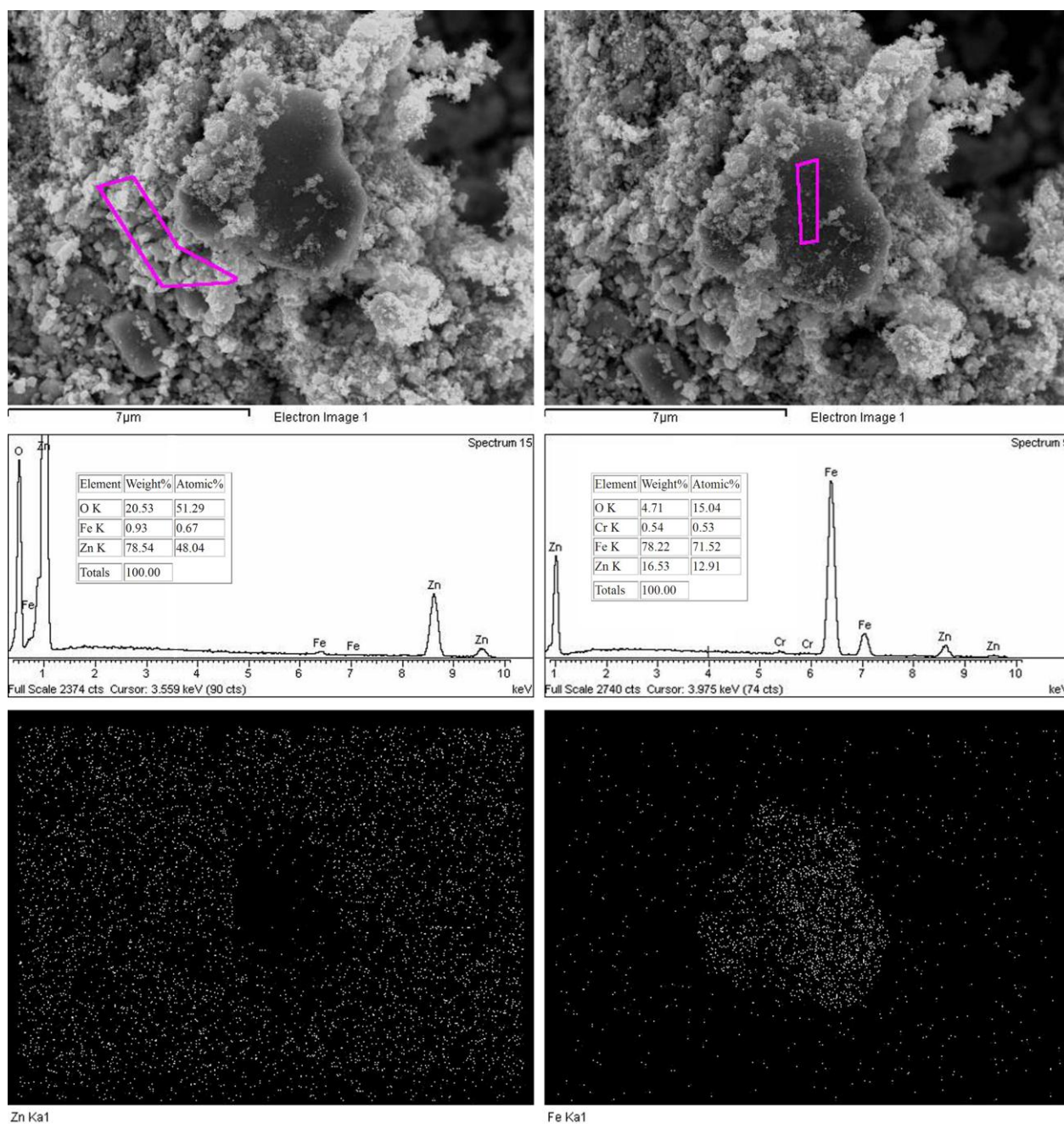
Fig. S24 FE-SEM micrograph of sample A2 obtained at 6500 × magnification with marked regions (top-left and top-right) used for the EDS analysis. The corresponding EDS spectra and the results of elemental analysis (inset tables) are shown below (middle-left and middle-right). EDS mapping of Zn (bottom-left) and Fe (bottom-right) are given below.

| Element	Weight%	Atomic%
O K	15.29	42.25
Cr K	0.41	0.35
Fe K	3.18	2.52
Zn K	81.13	54.88
Totals	100.00	

Fig. S25 FE-SEM micrograph of sample A5 obtained at 80 × magnification (top) and the corresponding EDS spectrum (bottom). Inset table shows the results of elemental analysis.

Element	Weight%	Atomic%
O K	15.82	43.13
Cr K	0.63	0.53
Fe K	4.94	3.86
Ni K	0.29	0.22
Zn K	78.32	52.27
Totals	100.00	

Fig. S26 FE-SEM micrograph of sample A9 obtained at 30 × magnification (top) and the corresponding EDS spectrum (bottom). Inset table shows the results of elemental analysis.

Element	Weight%	Atomic%
O K	15.17	41.86
Cr K	0.79	0.67
Fe K	6.04	4.77
Ni K	0.34	0.26
Zn K	77.66	52.44
Totals	100.00	

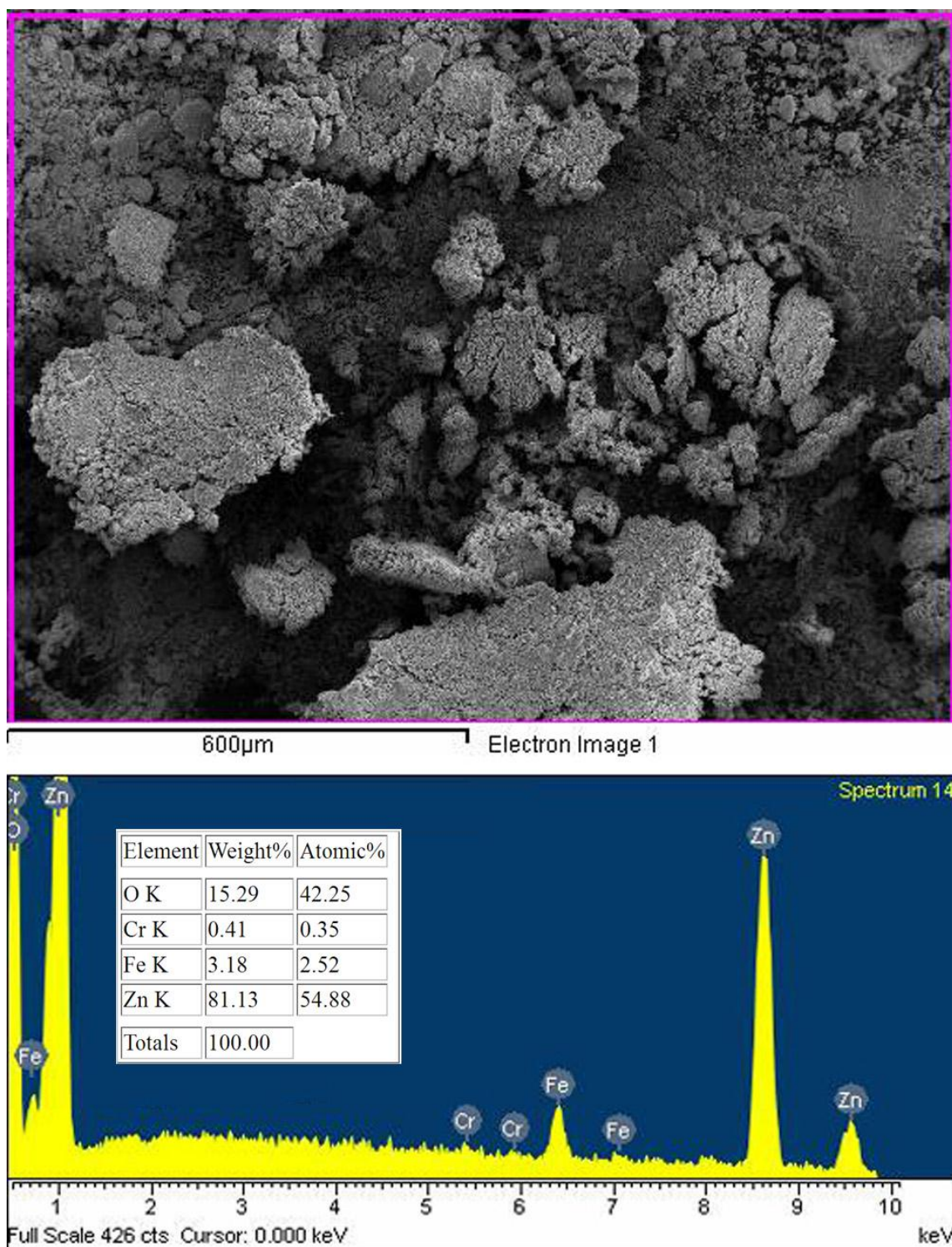Full Scale 182 cts Cursor: 10.121 keV (0 cts)

Fig. S27 FE-SEM micrograph of sample A14 obtained at 40 × magnification (top) and the corresponding EDS spectrum (bottom). Inset table shows the results of elemental analysis.

Element	Weight%	Atomic%
C K	1.46	4.70
O K	19.88	47.92
Cr K	1.09	0.81
Fe K	7.73	5.34
Ni K	0.57	0.37
Zn K	69.27	40.87
Totals	100.00	

Fig. S28 FE-SEM micrograph of sample A20 obtained at 230 × magnification (top) and the corresponding EDS spectrum (bottom). Inset table shows the results of elemental analysis.
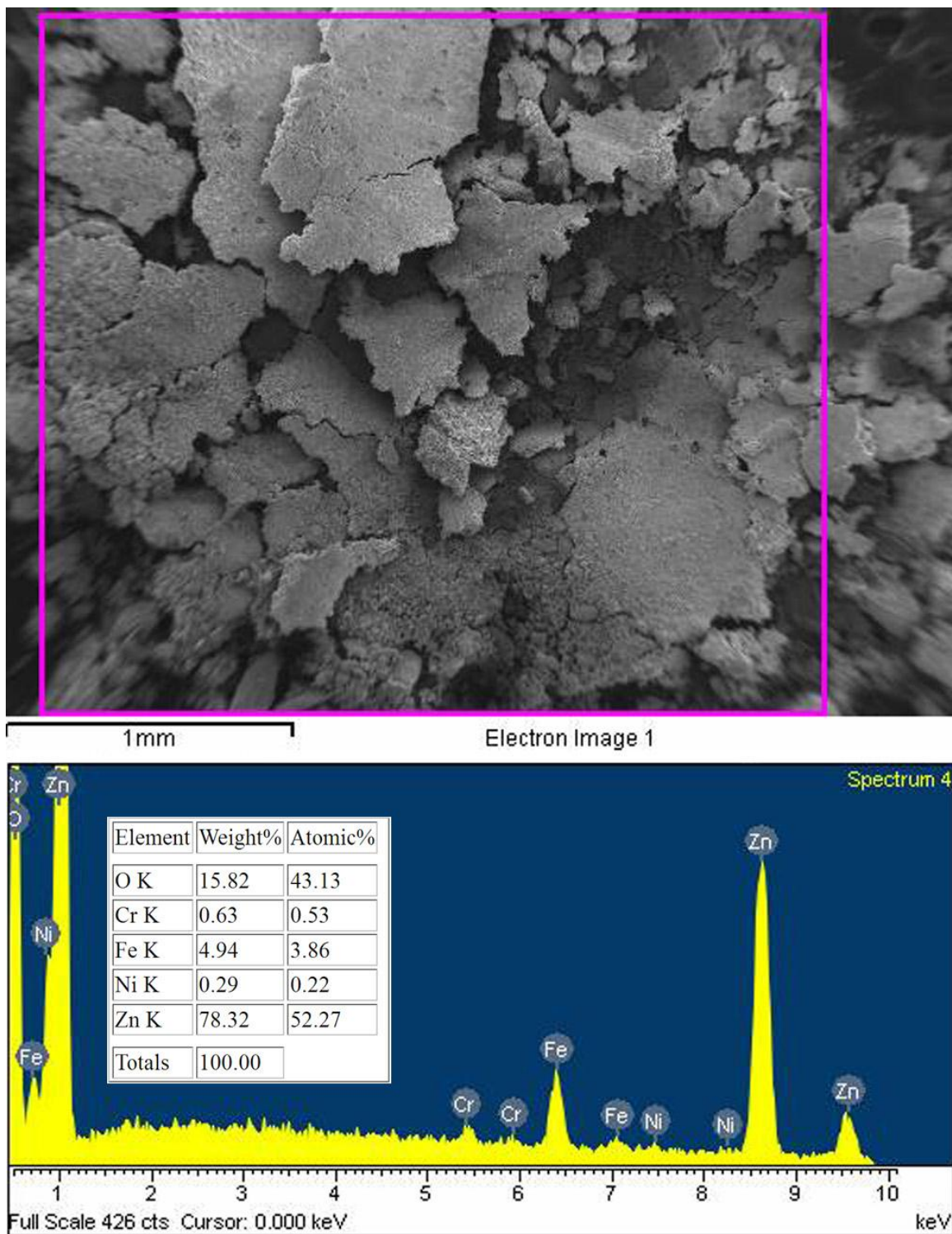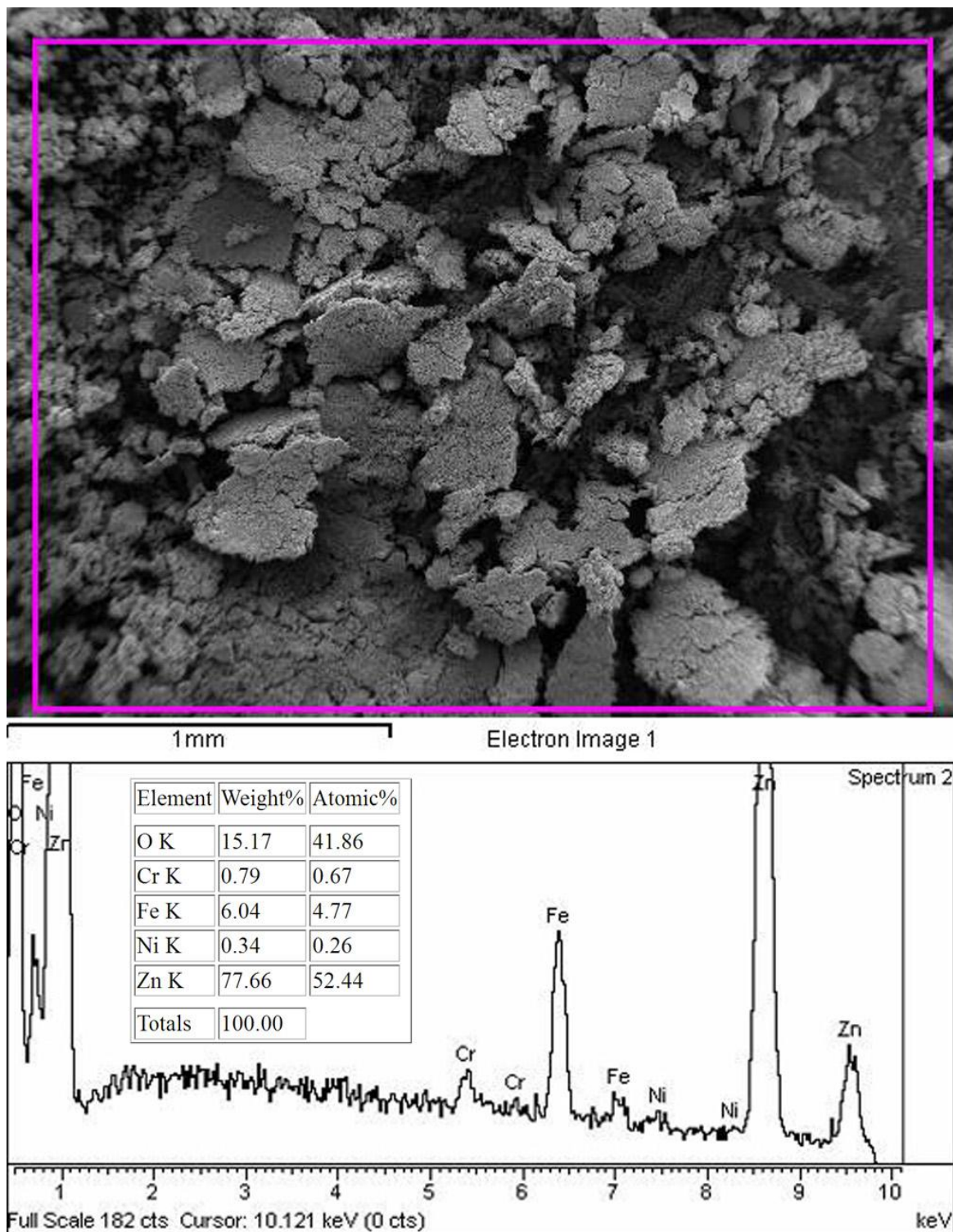
400μm   Electron Image 1

Element	Weight%	Atomic%
Cr K	1.25	0.95
Fe K	9.71	6.91
Ni K	0.79	0.54
Zn K	68.02	41.36
O	20.22	50.24
Totals	100.00	

Full Scale 1029 cts Cursor: 10.053 keV (0 cts)

Fig. S29 FE-SEM micrograph of sample A25 obtained at $100 \times$ magnification (top) and the corresponding EDS spectrum (bottom). Inset table shows the results of elemental analysis.
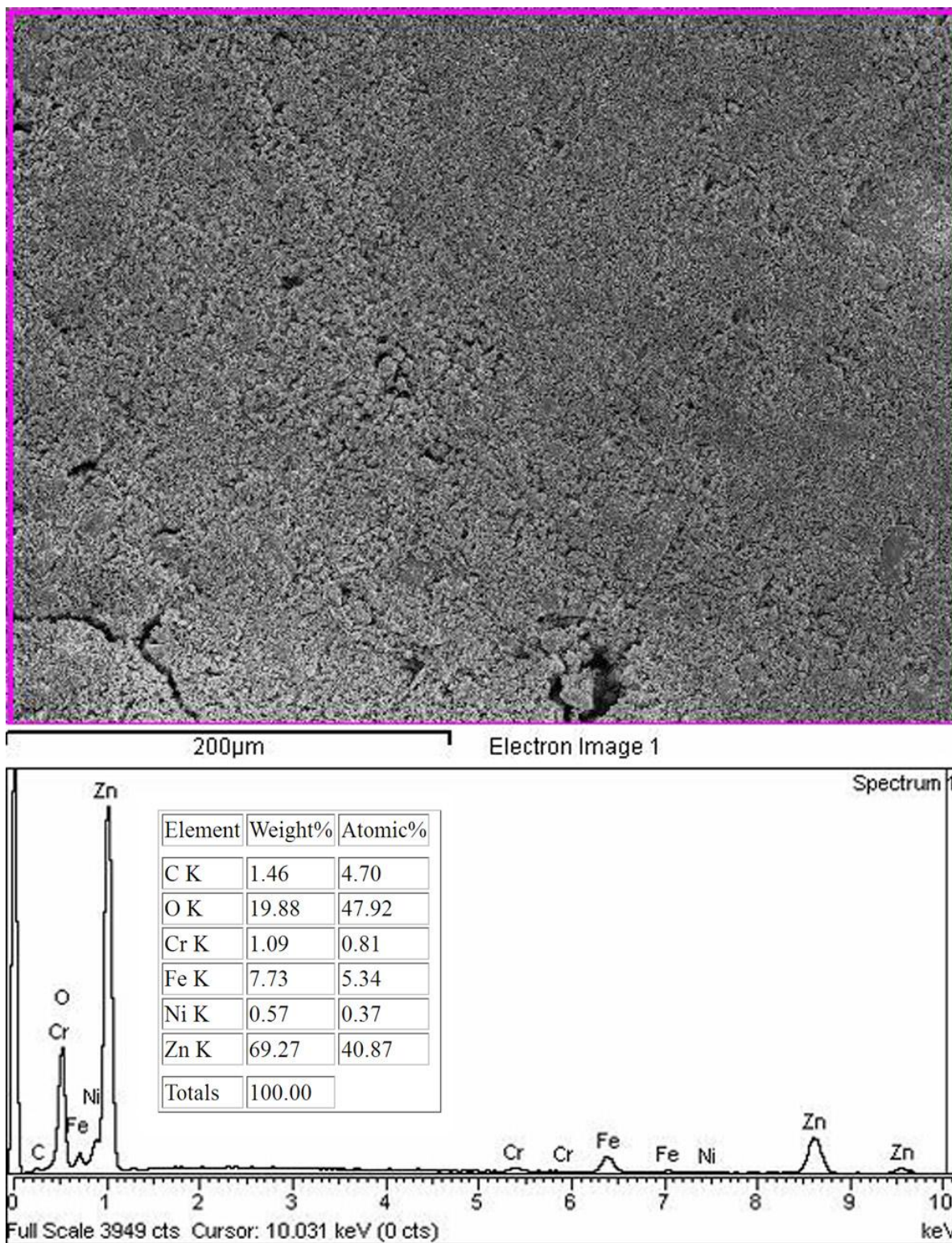
Element	Weight%	Atomic%
O K	17.29	45.37
Cr K	1.39	1.12
Fe K	10.90	8.19
Ni L	1.00	0.72
Zn K	69.42	44.59
Totals	100.00	

Fig. S30 FE-SEM micrograph of sample A30 obtained at 230 × magnification (top) and the corresponding EDS spectrum (bottom). Inset table shows the results of elemental analysis.
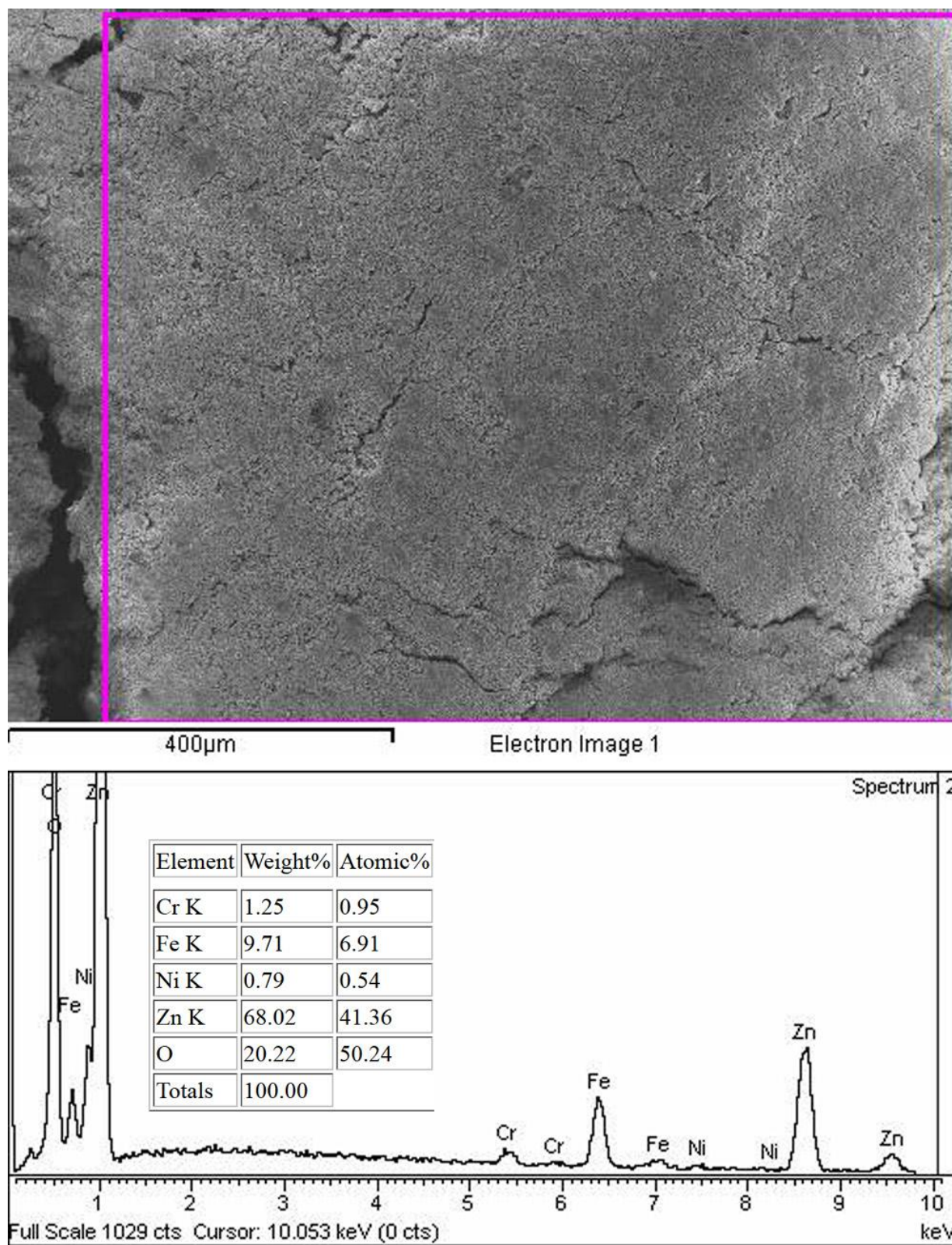
Element	Weight%	Atomic%
O K	16.15	43.32
Cr K	1.67	1.38
Fe K	11.99	9.21
Zn K	70.19	46.09
Totals	100.00	

Full Scale 426 cts Cursor: 0.000 keV

Fig. S31 FE-SEM micrograph of sample A30-500 obtained at 140 × magnification (top) and the corresponding EDS spectrum (bottom). Inset table shows the results of elemental analysis.
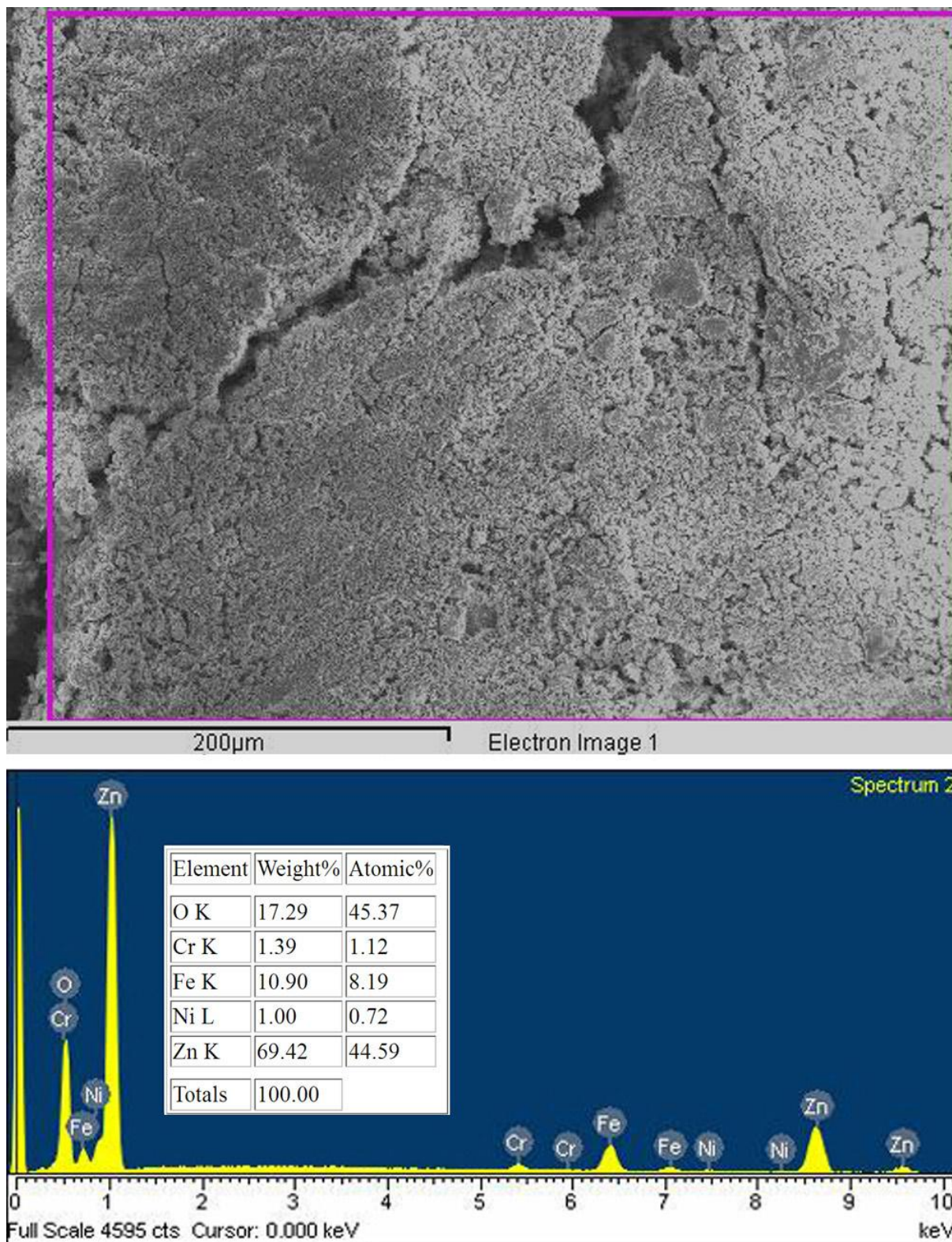
Element	Weight%	Atomic%
O K	16.35	43.67
Cr K	1.39	1.14
Fe K	12.03	9.21
Ni K	0.79	0.58
Zn K	69.44	45.40
Totals	100.00	

Fig. S32 FE-SEM micrograph of sample A30-1000 obtained at $65 \times$ magnification (top) and the corresponding EDS spectrum (bottom). Inset table shows the results of elemental analysis.
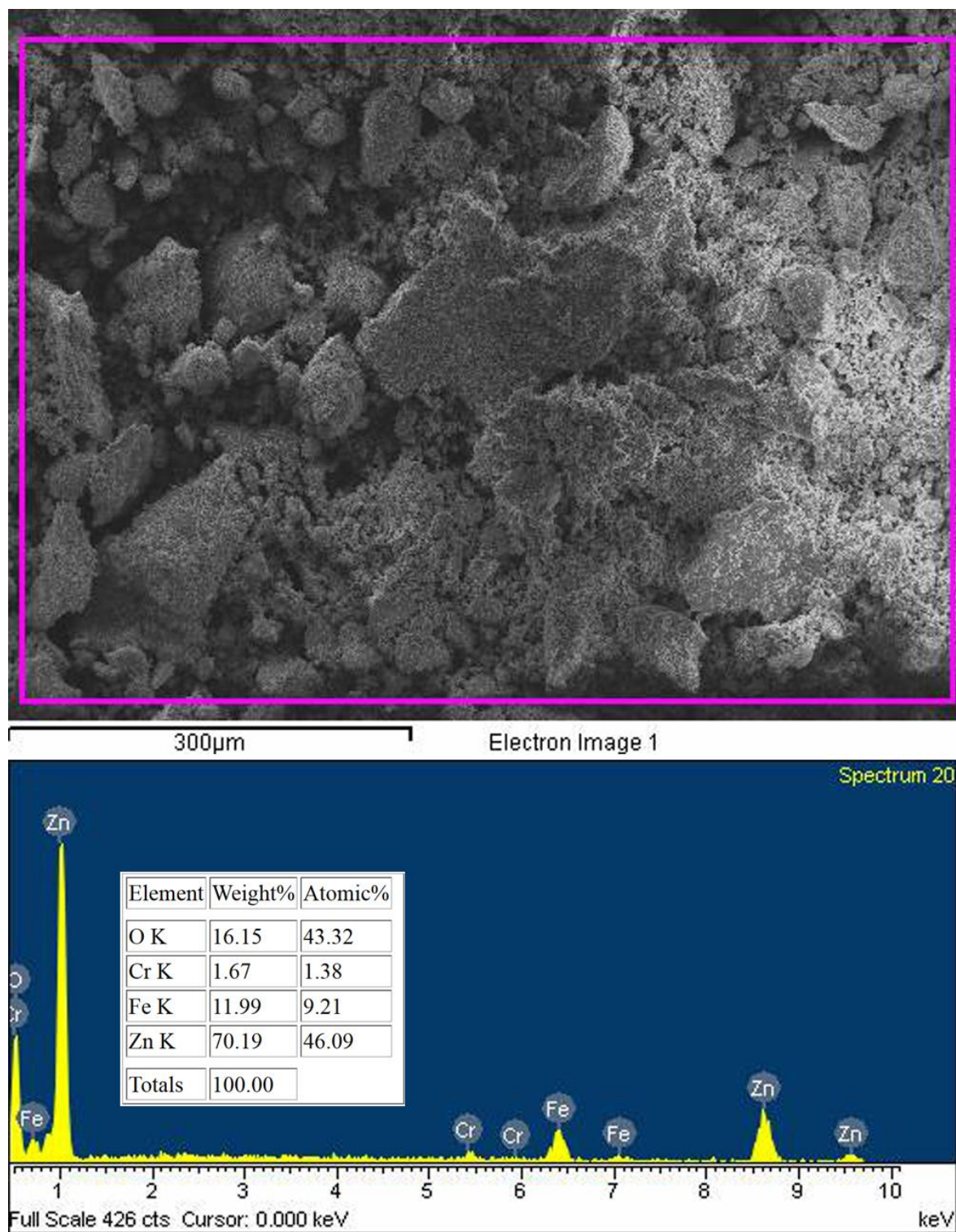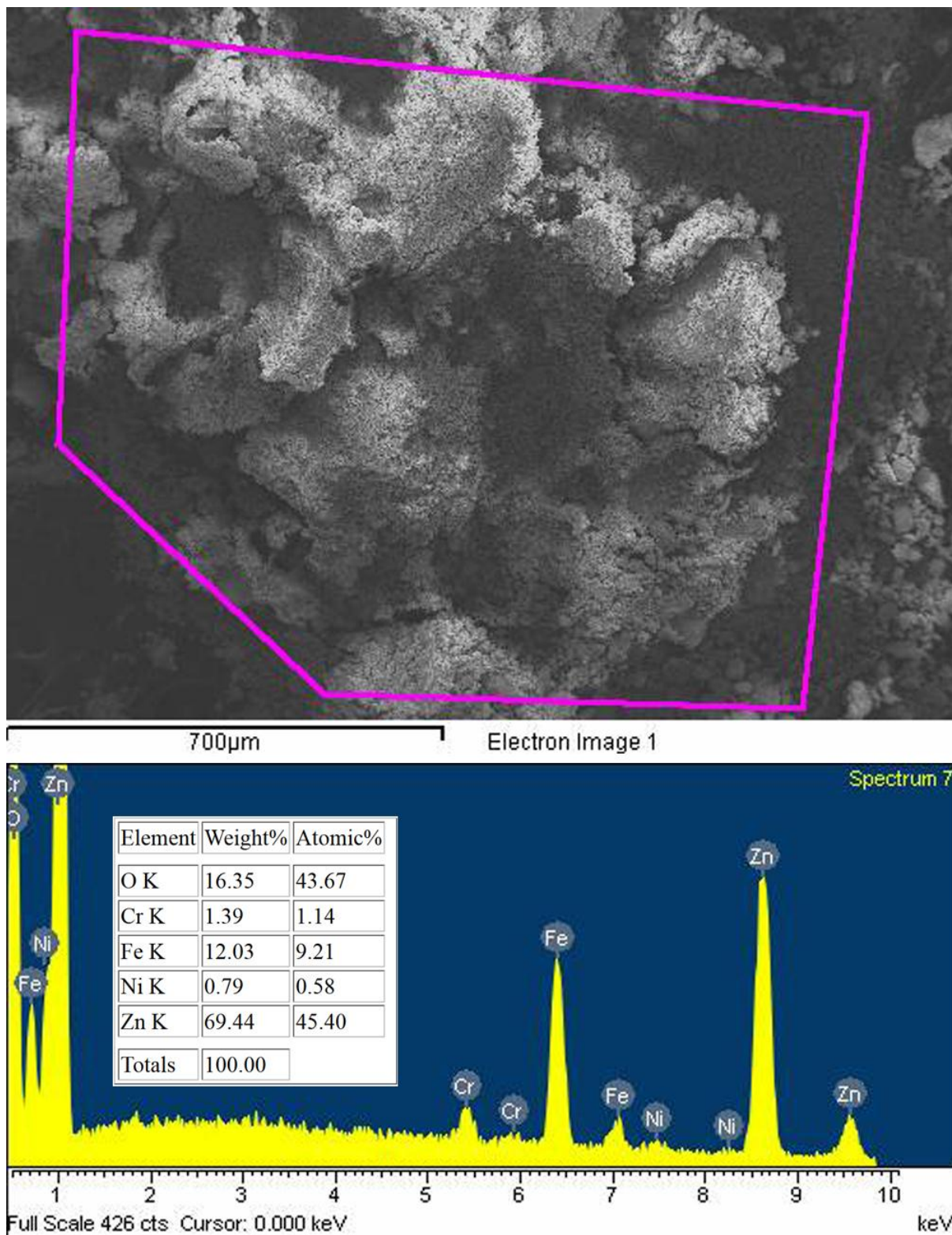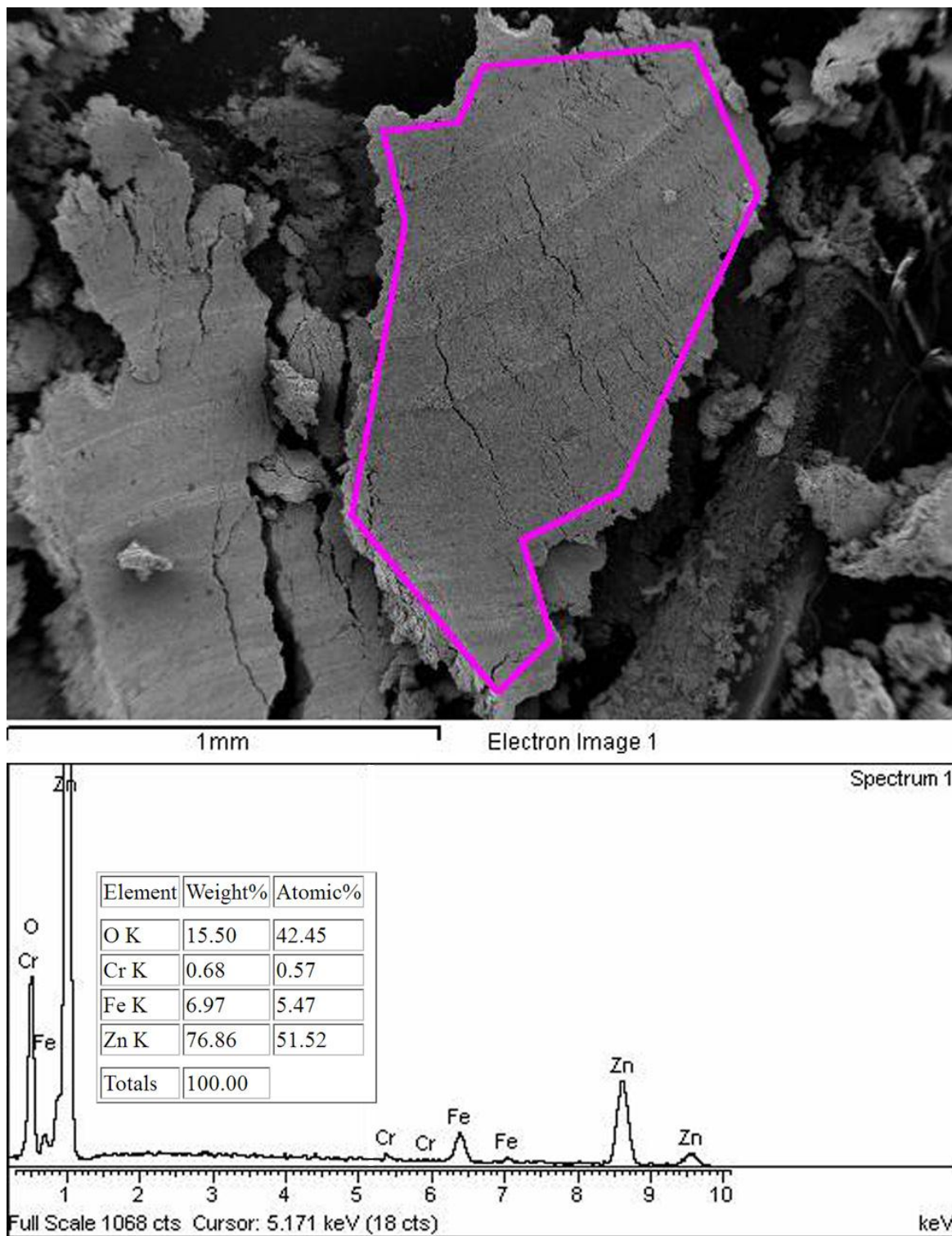
Element	Weight%	Atomic%
O K	15.50	42.45
Cr K	0.68	0.57
Fe K	6.97	5.47
Zn K	76.86	51.52
Totals	100.00	

Fig. S33 FE-SEM micrograph of sample B14 obtained at 45 × magnification (top) and the corresponding EDS spectrum (bottom). Inset table shows the results of elemental analysis.

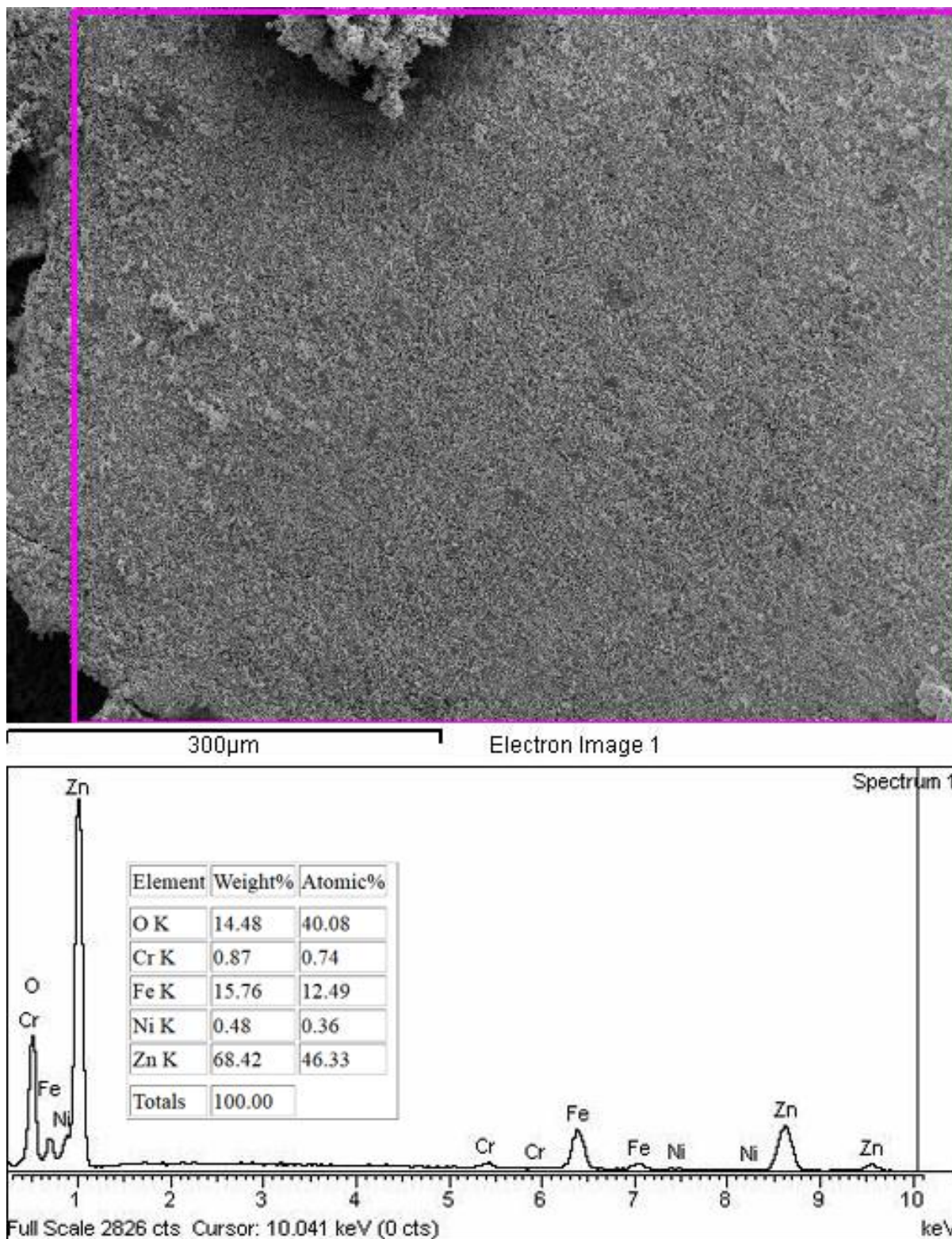| Element	Weight%	Atomic%
O K	14.48	40.08
Cr K	0.87	0.74
Fe K	15.76	12.49
Ni K	0.48	0.36
Zn K	68.42	46.33
Totals	100.00	

Fig. S34 FE-SEM micrograph of sample B30 obtained at 150 × magnification (top) and the corresponding EDS spectrum (bottom). Inset table shows the results of elemental analysis.

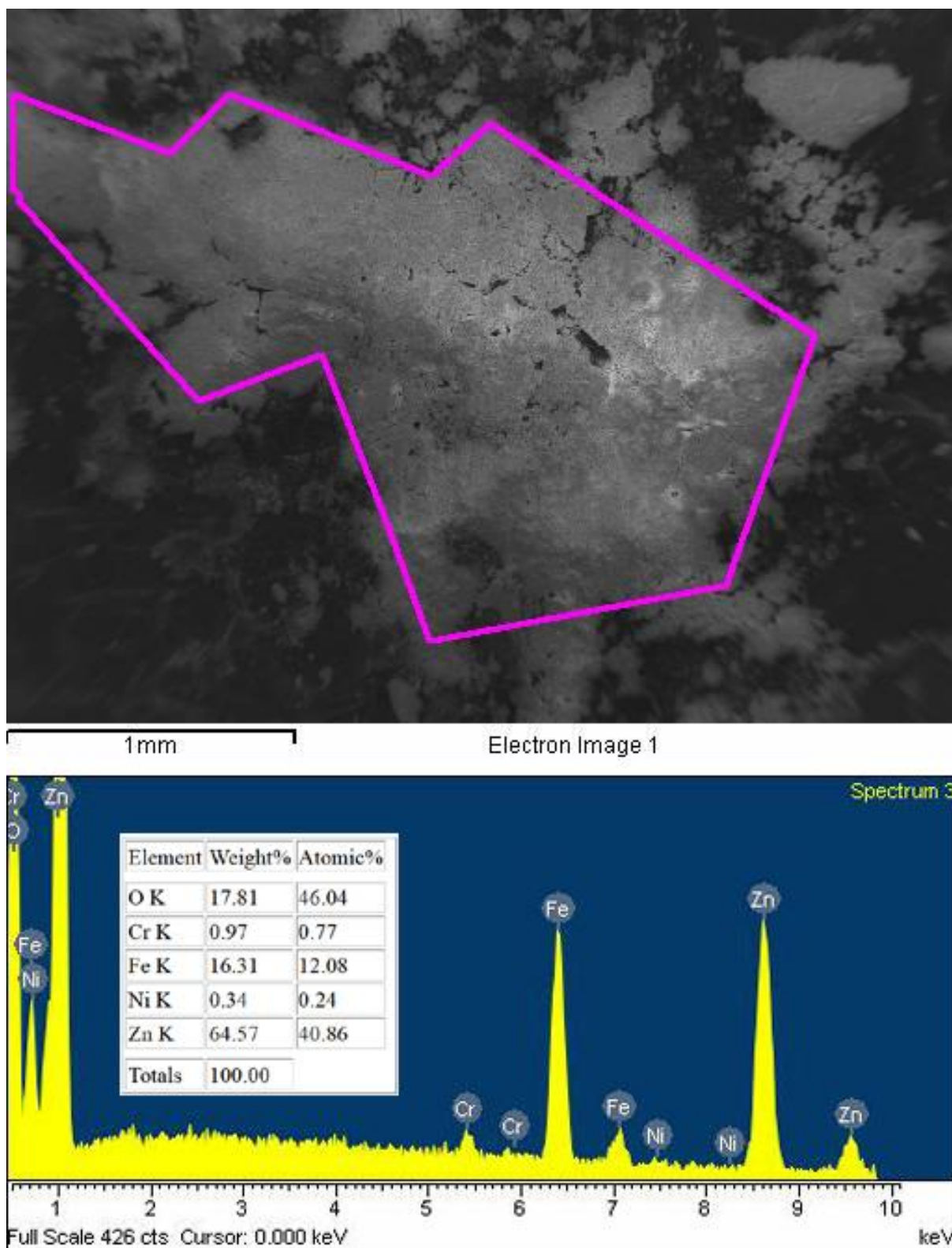| Element	Weight%	Atomic%
O K	17.81	46.04
Cr K	0.97	0.77
Fe K	16.31	12.08
Ni K	0.34	0.24
Zn K	64.57	40.86
Totals	100.00	

Fig. S35 FE-SEM micrograph of sample B30-500 obtained at 30 × magnification (top) and the corresponding EDS spectrum (bottom). Inset table shows the results of elemental analysis.

Element	Weight%	Atomic%
O K	17.31	45.17
Cr K	0.96	0.77
Fe K	16.95	12.67
Ni L	0.57	0.40
Zn K	64.21	41.00
Totals	100.00	

Fig. S36 FE-SEM micrograph of sample B30-1000 obtained at 95 × magnification (top) and the corresponding EDS spectrum (bottom). Inset table shows the results of elemental analysis.
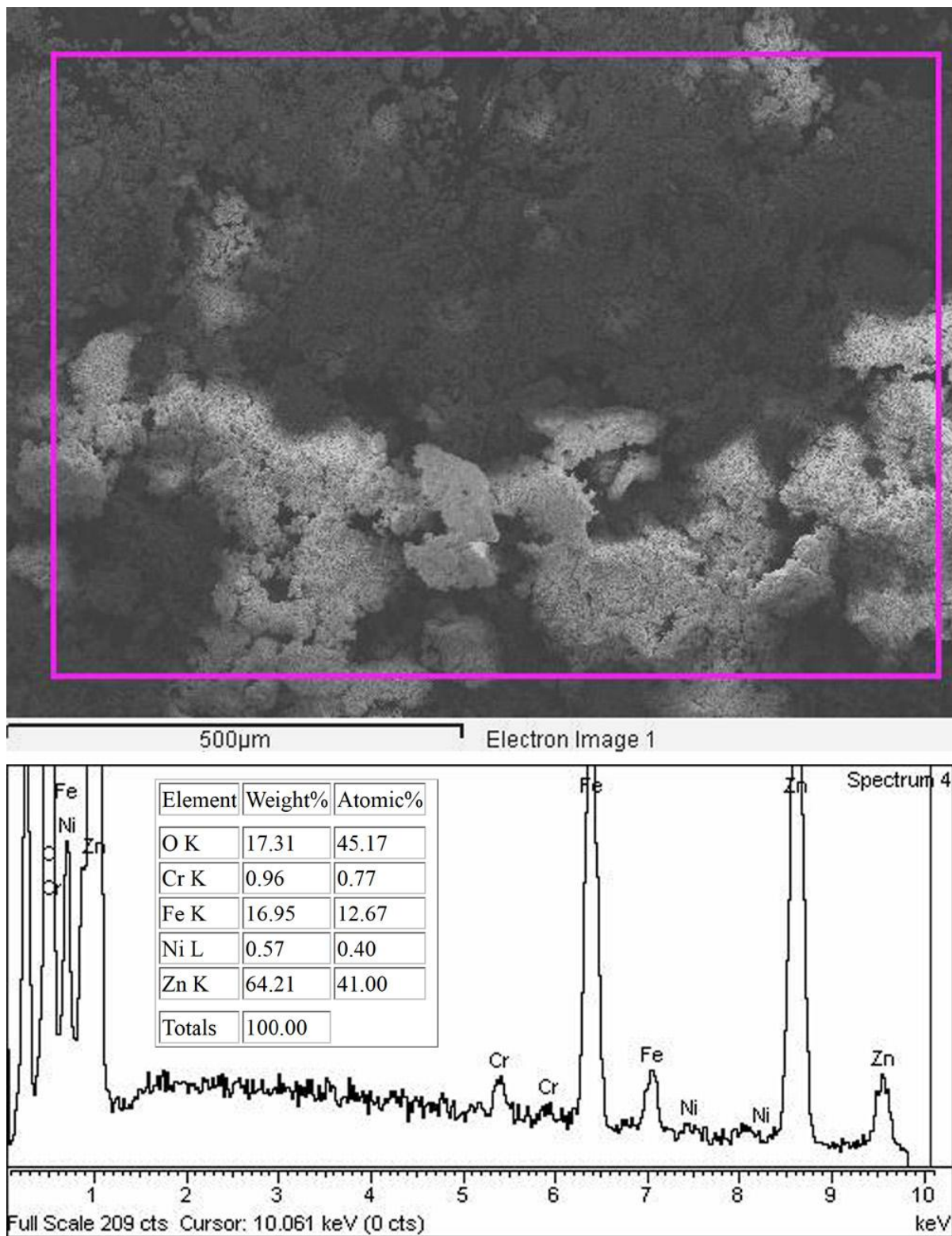
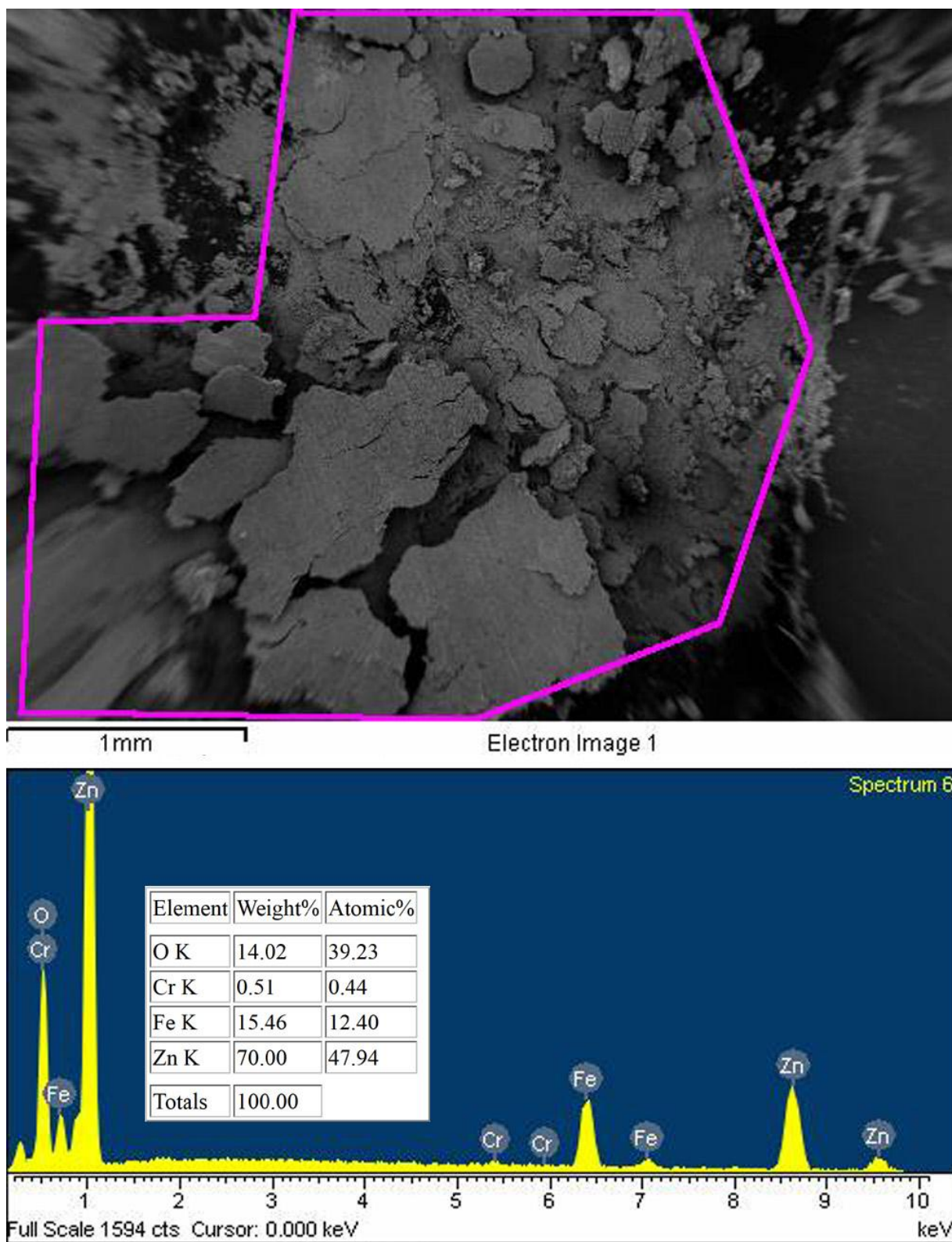| Element	Weight%	Atomic%
O K	14.02	39.23
Cr K	0.51	0.44
Fe K	15.46	12.40
Zn K	70.00	47.94
Totals	100.00	

Fig. S37 FE-SEM micrograph of sample C14 obtained at 25 × magnification (top) and the corresponding EDS spectrum (bottom). Inset table shows the results of elemental analysis.

Element	Weight%	Atomic%
O K	10.68	31.26
Cr K	0.79	0.71
Fe K	38.04	31.88
Zn K	50.49	36.15
Totals	100.00	

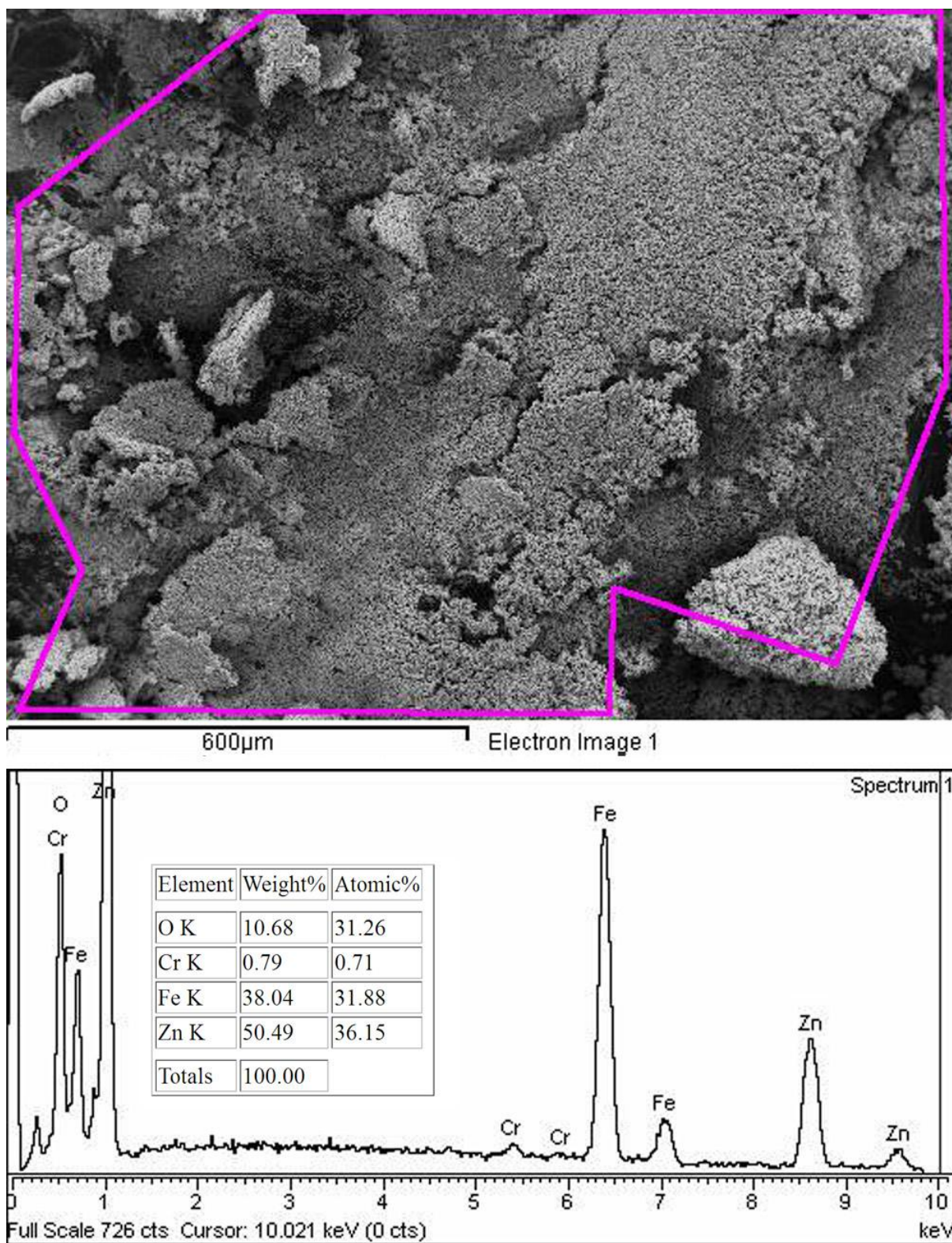Full Scale 726 cts Cursor: 10.021 keV (0 cts)

Fig. S38 FE-SEM micrograph of sample C30 obtained at 80 × magnification (top) and the corresponding EDS spectrum (bottom). Inset table shows the results of elemental analysis.
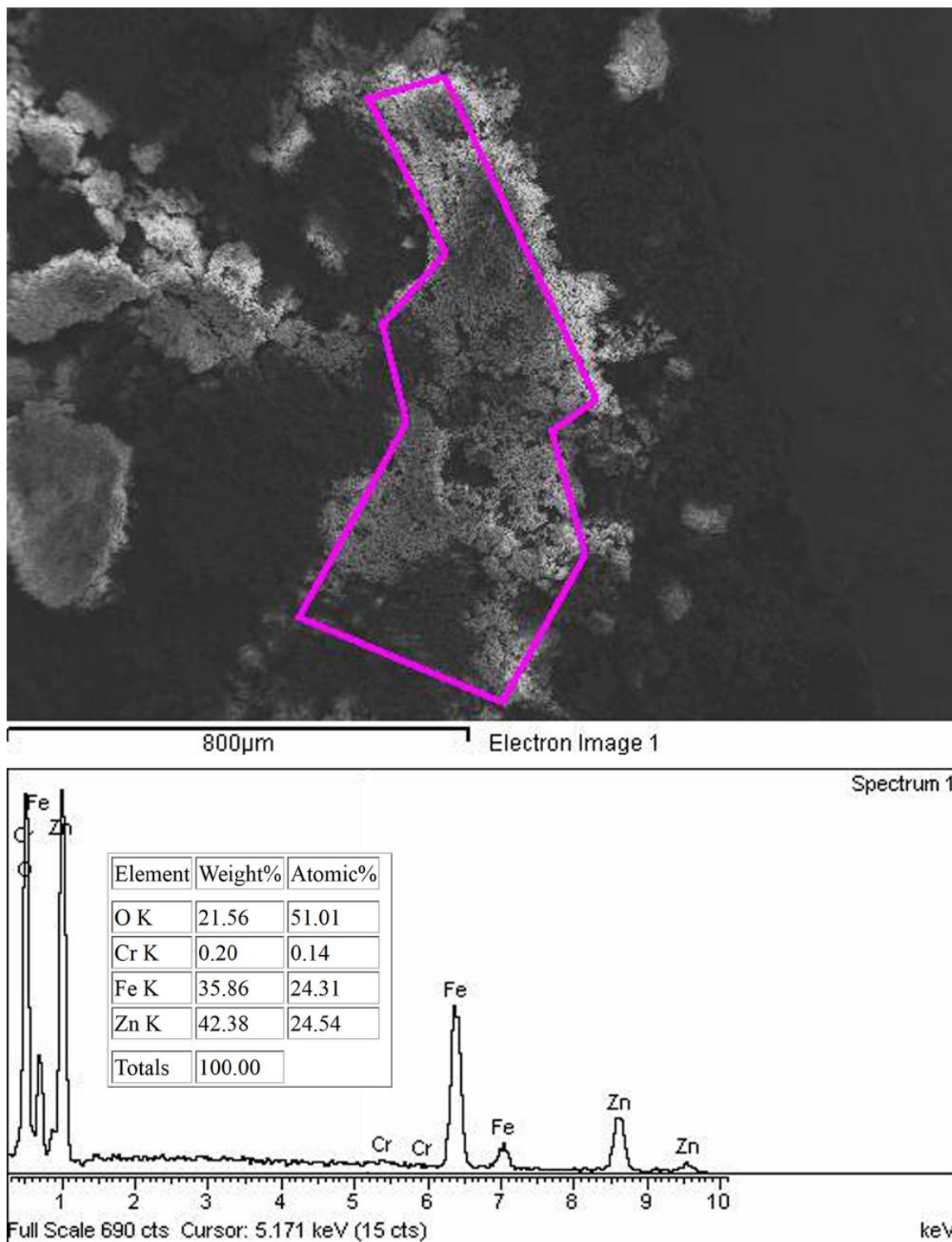
Fig. S39 FE-SEM micrograph of sample C30-500 obtained at $60 \times$ magnification (top) and the corresponding EDS spectrum (bottom). Inset table shows the results of elemental analysis.
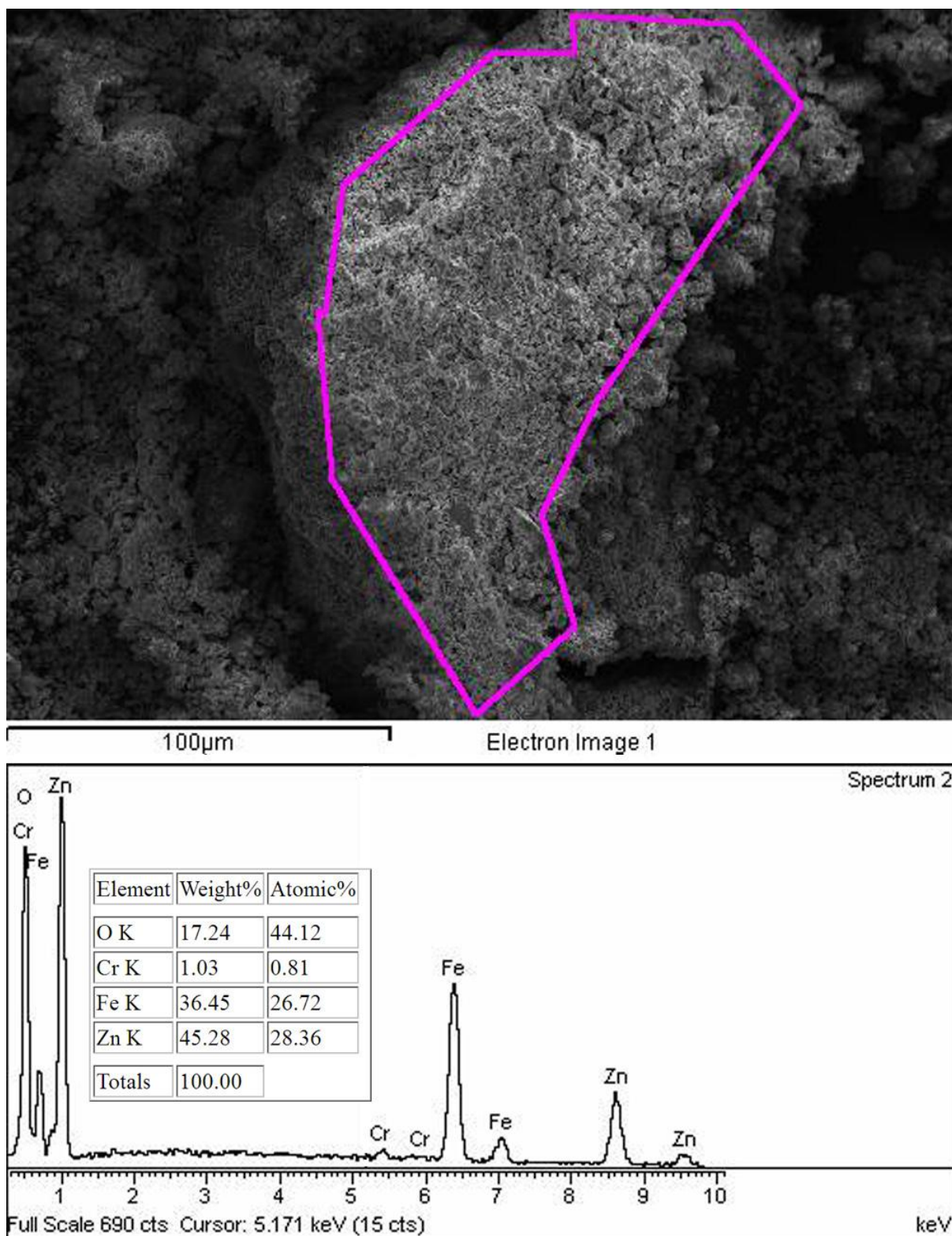
Element	Weight%	Atomic%
O K	17.24	44.12
Cr K	1.03	0.81
Fe K	36.45	26.72
Zn K	45.28	28.36
Totals	100.00	

Fig. S40 FE-SEM micrograph of sample C30-1000 obtained at 400 × magnification (top) and the corresponding EDS spectrum (bottom). Inset table shows the results of elemental analysis.

Fig. S41 The influence of ball-milling of pure zincite by procedures A, B and C and temperature treatment of the final milling products (30 h) on the amount of Fe and Cr contaminations as determined from the results of EDS analysis.
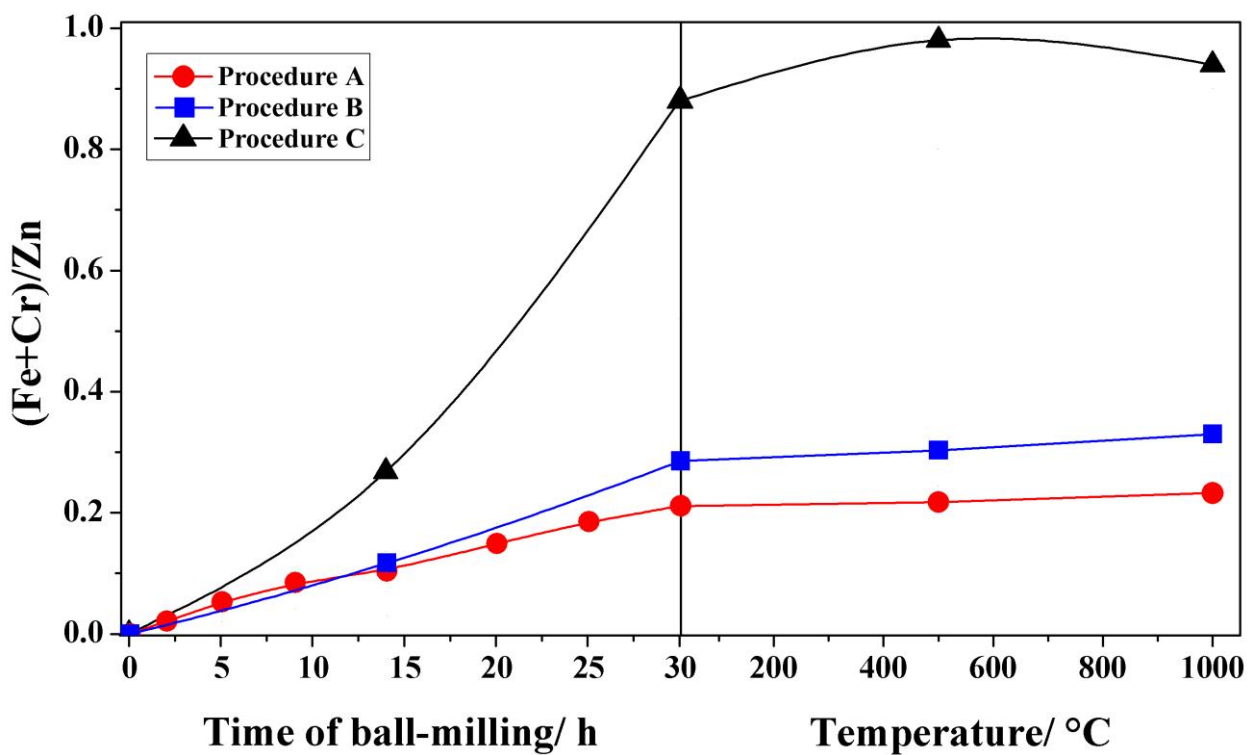
Fig. S42 The influence of ball-milling of pure zincite by procedures A, B and C and temperature treatment of the final milling products (30 h) on the amount of Fe and Cr contaminations as determined from the results of EDS (full symbols, solid lines) and XRD analysis (empty symbols, dash lines).
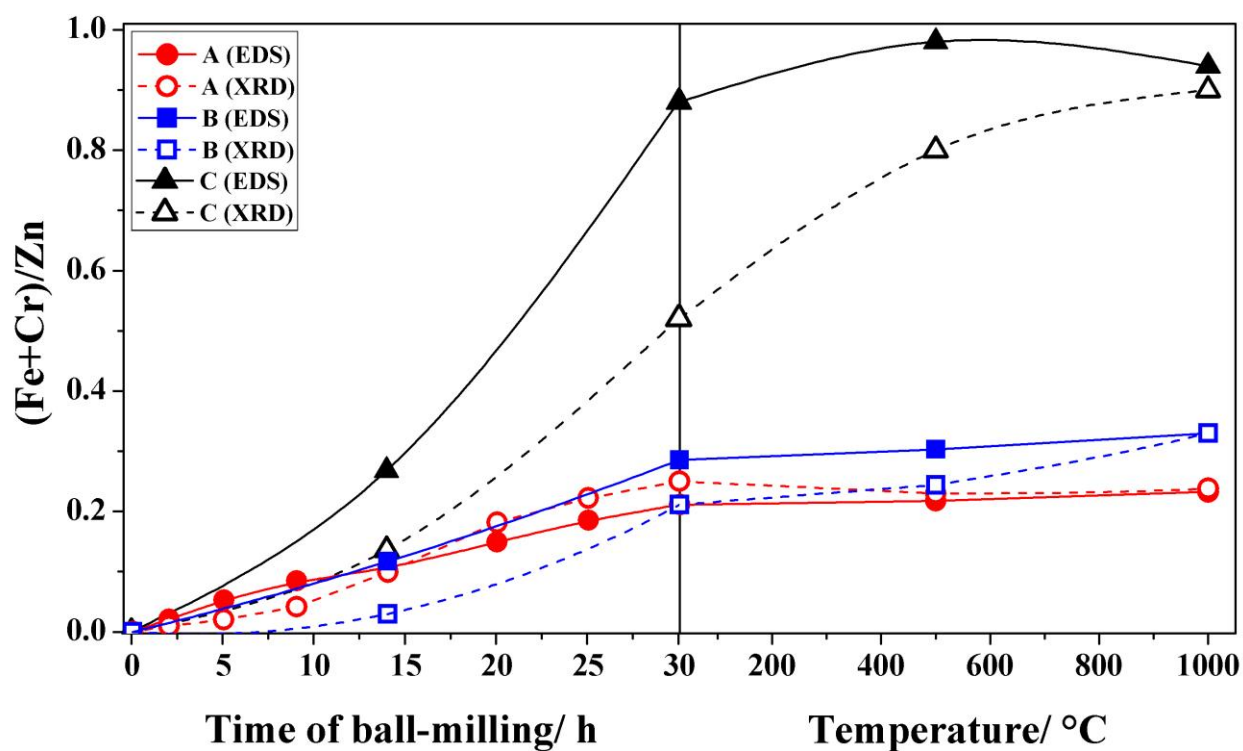
Fig. S43 The influence of ball-milling of pure zincite by procedures A and B and temperature treatment of the final milling products (30 h) on the amount of Fe and Cr contaminations as determined from the results of EDS (full symbols, solid lines) and XRD analysis (empty symbols, dash lines).
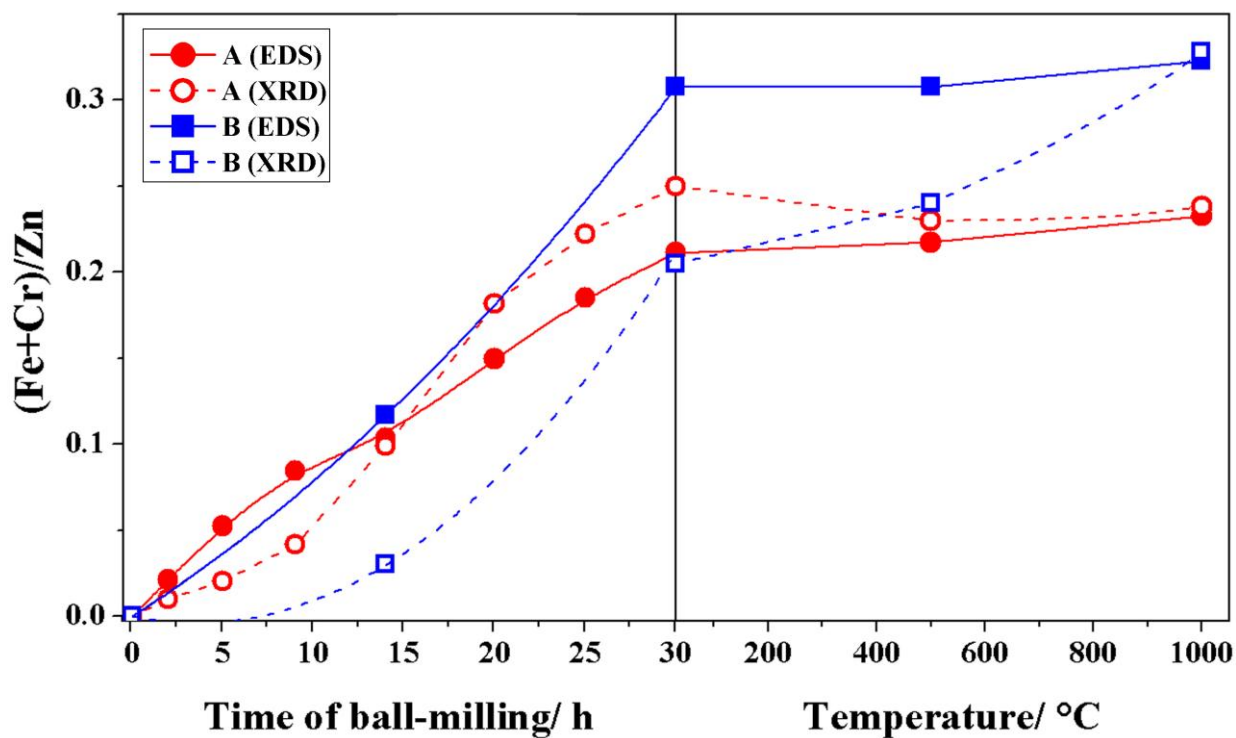
Table S5 The (Fe+Cr)/Zn ratio estimated from the results of EDS and XRD analysis and the percentage of contamination from the balls and vial as determined from the Cr/Fe ratio obtained from the results of EDS analysis. The (Fe+Cr)/Zn ratios estimated from the results of quantitative crystal phase analysis (XRD) were obtained by assuming formula ZnO, (Fe,Cr), (Fe,Cr)O and $Zn(Fe,Cr)_2O_4$ for the zincite-, iron-, wüstite- and franklinite-type phases, respectively.

Sample	(Fe+Cr)/Zn (EDS)	(Fe+Cr)/Zn (XRD)	Fe/Cr ratio	Cr/Fe ratio	Contaminatio (balls)/ %	Contaminatio (vial)/ %
vial	-	-	3.2	0.305	-	-
balls	-	-	58.9	0.017	-	-
A2	0.02	0.01	-	-	-	-
A5	0.05	0.02	7.2	0.139	57.6	42.4
A9	0.09	0.04	7.3	0.137	58.3	41.7
A14	0.10	0.10	7.1	0.141	56.9	43.1
A20	0.15	0.18	6.6	0.152	53.2	46.8
A25	0.19	0.22	7.3	0.137	58.3	41.7
A30	0.21	0.25	7.3	0.137	58.3	41.7
A30-500	0.22	0.23	6.7	0.149	54.0	46.0
A30-1000	0.23	0.23	8.0	0.125	62.5	37.5
B14	0.12	0.03	9.6	0.104	69.7	30.3
B30	0.31	0.20	16	0.063	84.2	15.8
B30-500	0.31	0.24	15.7	0.064	83.8	16.2
B30-1000	0.32	0.32	16.4	0.061	84.8	15.2
C14	0.27	0.14	28.2	0.035	93.6	6.4
C30	0.89	0.49	45	0.022	98.2	1.8
C30-500	0.97	0.80	58	0.020	99.9	0.1
C30-1000	0.93	0.88	50	0.020	99.0	1.0

Section S12 *References*

S1.   S. Linderoth, J. Z. Jiang, and S. Mørup, *Mater. Sci. Forum*, 1997, **235-238**, 205–210.

S2.   S. J. Campbell, W. A. Kaczmarek, and G.-M. Wang, *Nanostruct. Mater.*, 1995, **6**, 735–738.

S3.   G. F. Goya, H. R. Rechenberg, and J. Z. Jiang, *J. Appl. Phys.*, 1998, **84**, 1101–1108.

S4.   M. Menzel, V. Šepelák and K. D. Becker, *Solid State Ionics*, 2001, **141–142**, 663–669.

S5.   V. Šepelák, M. Menzel, K. D. Becker and F. Krumeich, *J. Phys. Chem. B*, 2002, **106**, 6672–6678

S6.   J. Ding, P. G. McCormick, and R. Street, *Journal of Magnetism and Magnetic Materials*, 1997, **171**, 309–314.

S7.   M. Hofmann, S. J. Campbell, W. A. Kaczmarek, and S. Welzel, *J. Alloys Compd.*, 2003, **348**, 278–284.

S8.   Č. Jovalekić, M. Zdujić, A. Radaković, and M. Mitrić, *Materials Letters*, 1995, **24**, 365–368.

S9.   J. Z. Jiang, Y. X. Zhou, S. Mørup, and C. Bender Koch, *Nanostruct. Mater.*, 1996, **7**, 401-410.

S10. V. G. Harris, D. J. Fatemi, J. O. Cross, E. E. Carpenter, V. M. Browning, J. P. Kirkland, A. Mohan, and G. Long, *J. Appl. Phys.*, 2003, **94**, 496–501.

S11. F. Padella, C. Alvani, A. La Barbera, G. Ennas, R. Liberatore, and F. Varsano, *Mater. Chem. Phys.*, 2005, **90**, 172–177.

S12. E. C. Reisdoerfer, F. F. Ivashita, J. V. Bellini, A. Paesano Jr., A. C. S. da Costa, S. A. Pianaro, and B. Hallouche, *Hyperfine Interactions*, 2009, **195**, 235–240.

S13. H. Dutta, Y.-C. Lee, and S. K. Pradhan, *Physica E*, 2007, **36**, 17–27.

S14. M. Jalaly, M. H. Enayati, F. Karimzadeh, and P. Kameli, *Powder Technology*, 2009, **193**, 150–153.

S15. M. Jalaly, M. H. Enayati, P. Kameli, and F. Karimzadeh, *Physica B: Condensed Matter*, 2010, **405**, 507–512.

S16. C. Jovalekić, A. S. Nikolić, M. Gruden-Pavlović, and M. B. Pavlović, *J. Serb. Chem. Soc.*, 2012, **77**, 497–505.

S17. H. M. Rietveld, *J. Appl. Cryst.*, 1969, **2**, 65–71.

S18. L. Lutterotti, S. Matthies and H.-R. Wenk, MAUD (Material Analysis Using Diffraction): A User Friendly Java Program for Rietveld Texture Analysis and More, in: Proceeding of

the Twelfth International Conference on Textures of Materials (ICOTOM-12), vol. 1, 1999, p. 1599.

S19. A. Le Bail, H. Duroy and J.L. Fourquet, *Mater. Res. Bull*., 1988, **23**, 447–452.

S20. A. C. Larson and R. B. Von Dreele, *General Structure Analysis System GSAS*, Los Alamos National Laboratory Report, 2001.

S21. B. H. Toby, *J. Appl. Cryst.,* 2001, **34**, 210–213.

S22. D. Balzar and H. Ledbetter, *J. Appl. Cryst.,* 1993, **26**, 97-103.

S23. B. E. Warren, *X-ray Diffraction* (Addison Wesley, Reading, MA, 1969).

S24. D. Balzar, ″BREADTH - a program for analyzing diffraction line broadening", *J. Appl. Cryst*., 1995, **28**, 244–245.

S25. S. A. Howard and R. L. Snyder, *Adv. X-ray Anal.,* 1983, **26**, 73–81.

S26. M.A. Valenzuela, P. Bosch, J. Jiménez-Becerrill, O. Quiroz and A.I. Páez, *J. Photochem. Photobiol. A*, 2002, **148**, 177–182.

S27. E. Murad and J. H. Johnston, *Iron Oxides and Oxyhydroxides* in: *Mössbauer Spectroscopy Applied to Inorganic Chemistry*, vol. 2, edited by G.J. Long, Plenum Publishing Corporation 1987, p. 507.

S28. L. Baum, M. Meyer, D. Richard, L.C. Damonte and L. Mendoza-Zélis, *Hyperfine Interact.,* 2007, **176**, 87-92.

S29. Y. Lin, D. Jiang, F. Lin, W. Shi and X. Ma, *J. Alloys Compd*., 2007, **436**, 30–33.

S30. L.C. Damonte, M. Meyer, L. Baum and L.A. Mendoza-Zélis, *Hyperfine Interact*., 2010, **195**, 227-233.

S31. H. Ehrhardt, S. J. Campbell and M. Hofmann, *J. Alloys Compd.*, 2002, **339**, 255–260.

S32. T. Verdier, V. Nivoix, M. Jean and B. Hannoyer, *J. Mater. Sci.*, 2004, **39**, 5151-5154.

S33. R. C. Mackenzie (ed.), *Differential Thermal Analysis Vol. 1*, Academic Press, London, 1970, p. 331.

S34. K. Morishige, S. Kittaka , T. Moriyasu and T. Morimoto, *J. Chem. Soc., Faraday Trans.*, 1980, **76**, 738-745.

S35. G. Štefanić, S. Musić and M. Ivanda, *J. Mol. Struct.*, 2009, **924-926**, 225-234.